Supplementary Information for, "More is Different: Mobile Ions Improve the Design Tolerances of Perovskite Solar Cells"

Hart, L. J. F.*, Angus, F.J., Li, Y., Khaleed, A., P. Calado, Durrant, J. R., Djurišić, A. B., Docampo, P.*, and Barnes, P. R. F.*

L. J. F. Hart, Dr P. R. F Barnes

Department of Physics and Centre for Processable Electronics, Imperial College London, South Kensington, U.K.

L. J. F. Hart, Professor J. R. Durrant

Department of Chemistry and Centre for Processable Electronics, Imperial College London, 82 Wood Lane, London, U.K.

F. J. Angus, Dr P. Docampo

Department of Chemistry, University of Glasgow, University Avenue, Glasgow, U.K.

Professor A. B. Djurišić, Y. Li, A. Khaleed

Department of Physics, The University of Hong Kong, Pokfulam Road, Hong Kong S.A.R, China

Professor J. R. Durrant

SPECIFIC IKC, College of Engineering, Swansea University, Bay Campus, Fabian Way, Swansea, U.K.

Dr P. Calado

Department of Engineering, The Open University, Walton Hall, Milton Keynes, U.K.

Email: lucy.hart18@imperial.ac.uk; pablo.docampo@glasgow.ac.uk; piers.barnes@imperial.ac.uk

Table of Contents

Extended Methods

Please note that reference numbers in this section refer to references in the main text.

1. Drift-Diffusion Simulations

Device simulations were performed using Driftfusion, a software package designed to model one-dimensional, ordered semi-conductor devices which contain up to two species of mobile ions.[26] Driftfusion models ionic carriers in the perovskite layer as Schottky defects, following the results of quantum mechanical calculations by Walsh et al.[44] This means that each mobile ion is compensated for by a counter-ion of opposite charge, which is assumed to be static. Here, we included a single, positively charged mobile ionic species to reflect experimental and theoretical work which suggests that halide vacancies are the ionic carrier with the highest concentration and conductivity in metal halide perovskites.[3-9] Additionally, we assumed that the mobile cations are restricted to the perovskite layer and neglected the electrochemical processes which may occur at perovskite/TL interfaces. Both these processes could alter interfacial recombination kinetics and/or lead to irreversible degradation of the perovskite crystal structure. The effect of such degradation is not explicitly included in our model though, assuming its consequence would be to increase surface recombination velocity, **Figure S3** suggests that this would decrease V_{OC}, potentially to the extent that $V_{OC} < V_{flat}$, with the result that ions start to reduce V_{OC}.

In order to determine an accurate value for V_{OC} in the simulations which included mobile ions, it was necessary to ensure that the ions were at steady state at each point along the JV curve, which we did by using a scan rate of 0.1 mV s^{-1}. Thus, the JVs simulated herein are not representative of device performance as conventionally measured during a JV scan (typically done at scan rates ~10-100 mV s^{-1}), but instead accurately describe how the simulated device behaves once the ionic charge has re-equilibrated in response to the applied bias. This means that the V_{OC} values we report are those of the fully stabilised device and any enhancement of V_{OC} in the presence of mobile ions is due to their impact upon the PSC's electrostatics, as opposed to being a transient effect. JV scans on the 1.6 eV bandgap perovskite were performed at 1 Sun equivalent illumination and those on the 1.5 eV bandgap perovskite were done at 1.2 Sun equivalent, to account for the increased absorption of the narrower bandgap active layer. This was done as the *n* and *k* values for of the perovskite composition used in ref. [2] could not be found in the literature. Given the 3 μs Shockley-Read-Hall lifetime used in these simulations (see **Table S2**) the effective diffusion length far exceeds the layer thickness. Consequently, the differences in generation rate profile will have negligible impact on the results.

To perform the simulations in which we varied ΔE_{TL}, the offsets at both interfaces were changed in a symmetric manner, while ensuring that the intrinsic carrier densities in both types of transport layer remained constant (asymmetric values of ΔE_{TL} are considered in **Supplementary Note One**). Where possible, V_{BI} was set to 1.1 V, though this had to be reduced for larger ΔE_{TL} values as Driftfusion cannot model situations where the electrode work function lies within the conduction or valance band of the transport layers.

To simulate the Stabilise and Pulse protocol, we first generated a series of solutions in which we allowed the ion distribution to reach its equilibrium position for the chosen V_{bias} value. Following this stabilisation, we then set the ionic mobility of each solution to zero to ensure that the ions were frozen in place during subsequent simulation. These solutions were then analysed using two different methods. In the first method, we performed an explicit simulation of the experimental protocol in which we took the input solution and ramped it to the desired V_{pulse} value over a time of 0.8 ms. We then held the device at V_{pulse} for 1 ms before recording the current output of the device. The ramp and dwell time were taken from the values stated in ref. [39] and this simulation protocol is akin to the one described in that work. However, this method was computationally costly, which limited the number of V_{pulse} values which it was feasible to simulate, leading to a relatively low voltage resolution. Thus, we also implemented a second method in which we took the stabilised, 'frozen-ion' solutions at each V_{bias} value and performed regular JV sweeps on them, the results of which agreed with those of the more explicit simulation protocol described above, and which allowed us to obtain a much higher resolution along the voltage axis (see **Figure S18**). The device efficiency for both the frozen ion and steady state JV curves was evaluated using PCE = $J_m V_m / P$ here J_m and V_m are the current density and voltage at the maximum power point on the JV curve, and P is the light intensity incident on the device.

2. Stabilise and Pulse Measurements

Initially, JV curves for each device were measured under standard AM1.5 simulated sunlight, as described in the Experimental section of the main text. Devices were then immediately transferred to the home-built Stabilise and Pulse setup. Here, a Cree High Power white LED was used as the light source, the intensity of which was calibrated to match the device's measured short circuit current density. Voltage pulses were provided by an Ossila Source Meter Unit. Each voltage pulse had a duration of approximately 40 ms and the device was stabilised for 1 s between the voltage pulses i.e., a duty cycle of around 5%. The source delay was set to 1 μs, meaning that the current value was acquired approximately 1 μs after the arrival of the voltage pulse, though we note that the returned value is the average over the following 15 μs. When changing the bias voltage, 50 mV step increments were used with the stabilisation period being a minimum of 120 s, though in some cases this was extended to obtain a stable current output. We note that devices using the alloyed perovskite required a longer

stabilisation period than those using MAPI. Consequently, the measurements were performed at approximately 0.5 Suns to prevent degradation during the significantly longer Stabilise and Pulse protocol.

In the main text, we show results extending up to the smallest V_{bias} value necessary to determine the quasi-steady state (QSS) V_{OC} as we found that the current did not stabilise prior to performing the pulsed JVs at higher values of V_{bias}, in contrast to what was observed for lower values of V_{bias} (see **Figure S5**). Based on the fact that this effect was smaller in the devices which included C_{60}-BA, we believe that this instability is related to electrochemical processes which occur at the TiO_2/MAPI interface following prolonged illumination (though we note that the SnO_2/MAPI interface is similarly affected, see **Supplementary Note Four**). This interpretation is supported by our observation of a slight reduction in device performance after collecting the Stabilise and Pulse data (see **Figure S19**). However, during the pulsed JVs themselves, the ionic configuration remained stable, as we demonstrate in **Figures 2a-b** which include Stabilise and Pulse data from the forward and reverse scan directions (see also **Figure S20**). The negligible amount of hysteresis strongly suggests that there is no ionic motion during the pulsed JV measurement.

A V_{flat} value was extracted from the Stabilise and Pulse data by analysing the gradient around the open circuit voltage of the JV obtained at each pre-bias voltage (V_{bias}). To find the gradient of each JV, a polynomial to the third degree was fitted to the 2-3 points above and below open circuit voltage and the gradient extracted from this fitting. Following this, we plotted the gradient around V_{OC} ($dJ/dV|_{V=Voc}$) against V_{bias}. To extract the V_{flat} value from this curve, we aim to identify the inflection point. The reasoning for this is that the inflection point will be the point where a change in states is observed, or rather a flipping in device behaviour, i.e., from being below V_{flat} to above V_{flat}. To find the inflection point, we first calculate the mean value of the steepest section of the plot by taking the average value of the two plateaus in $dJ/dV|_{V=Voc}$ (one at low bias, the other at high bias, see **Figure S8**). We then perform a linear regression on the section of the $dJ/dV|_{V=Voc}$ around this mean value. Finally, we extend this linear regression to find the points where it intercepts the values of $dJ/dV|_{V=Voc}$ at the high and low voltage plateaus. The mean value of these intercepts is then used to estimate V_{flat} for the device. We note that the reduction in device performance observed at high light intensities for the TiO_2 and SnO_2 devices without C_{60}-BA may lead to an underestimation of V_{flat}, by reducing the voltage at which the high voltage plateau in $dJ/dV|_{V=Voc}$ occurs. However, we do not believe that this has significantly impacted our results as we find similar values of V_{flat} in the devices which included C_{60}-BA, which did not show a significant reduction in performance at high forward bias. However, for this reason we have concentrated on the role of C_{60}-BA as a trap state passivator rather than any modulation of V_{flat} in the simulations shown in **Supplementary Note Three**.

Supplementary Figures

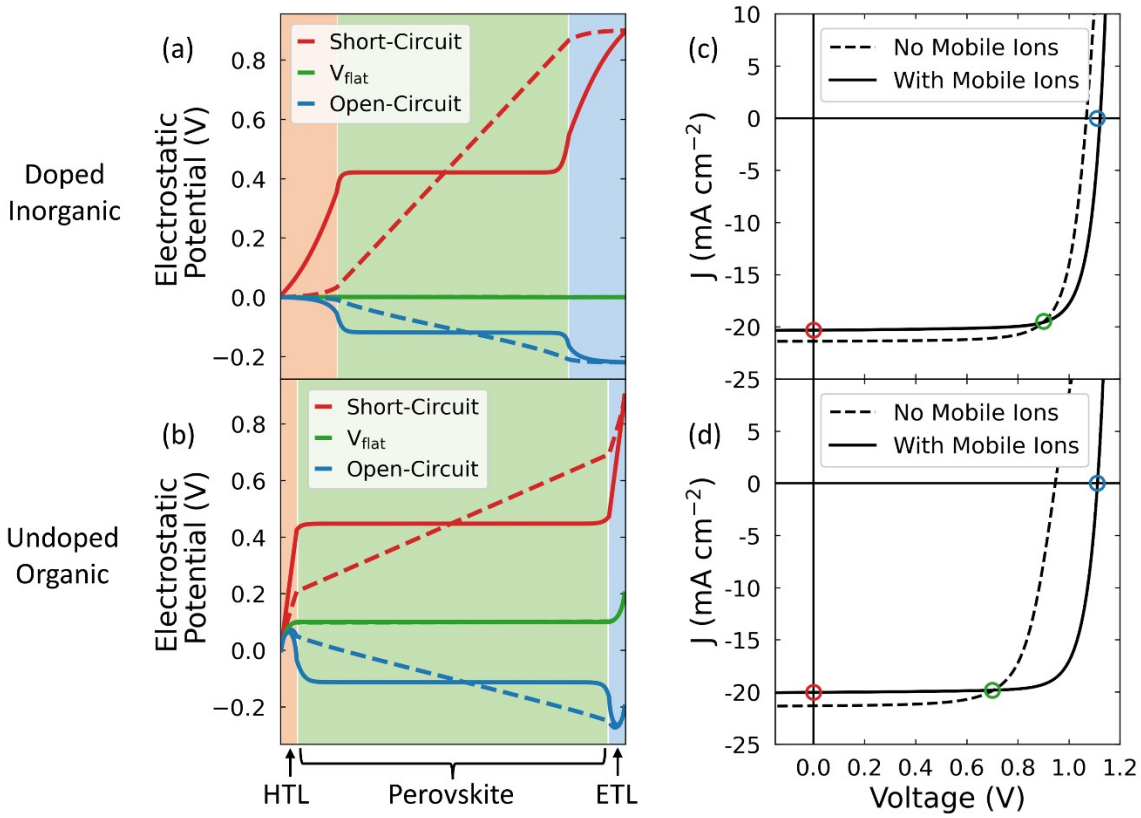

Figure S1: Figures (a) and (b) show the electrostatic potentials from the simulations shown in (c) and (d), which correspond to the doped inorganic and undoped organic parameters sets, respectively. Solid lines show the results when mobile ions are included ($N_{ion} = 10^{18}$ cm^{-3}) and dashed lines indicate results with no mobile ions. For both parameter sets, we used $\Delta E_{TL} = 0.25$ eV, $V_{BI} = 0.90$ V, and a surface recombination velocity of 10 cm s^{-1}. Electrostatic potentials are shown at short circuit (red, $V_{app} = 0$ V), the flat band condition in the perovskite (green, $V_{app} = 0.90$ V in figure (a) and $V_{app} = 0.70$ V in figure (b)) and open circuit for the device including mobile ions (blue, $V_{app} = 1.12$ V in figure (a) and $V_{app} = 1.11$ V in figure (b)). In both cases, we see that the inclusion of mobile ions increases the fraction of the electrostatic potential which is lost across the transport layers. Additionally, note how the use of undoped organic transport layers reduces V_{flat} by 0.2 V. Figures (c) and (d) show simulated steady state JV scans performed with and without the inclusion of a mobile ionic species for the doped inorganic and undoped organic parameter sets, respectively. Red, blue, and green circles correspond to the same potentials as shown in figures (a) and (b). Note that V_{flat} (as indicated by the green circles) is also the voltage at which the JV curves with and without mobile ions intersect as this is the only point in the JV scan where the electric field distribution, and thus electronic carrier distribution, are identical.

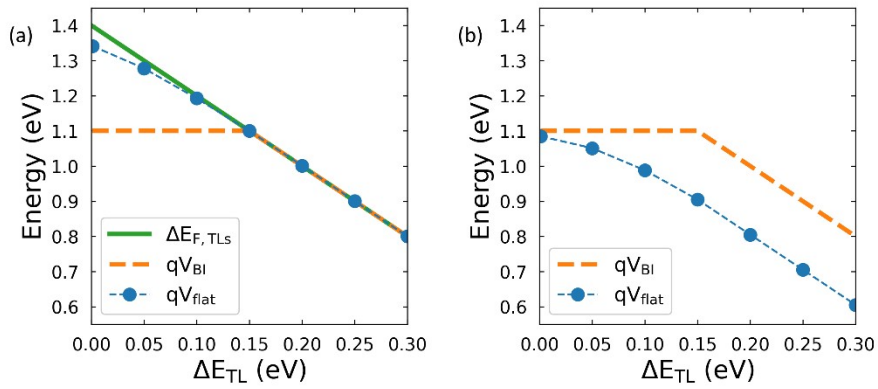

Figure S2: (a) The offset between the transport layers' equilibrium Fermi levels ($\Delta E_{F,TLs}$), the built in voltage (V_{BI}) and the flat band condition in the perovskite (V_{flat}) as a function of transport layers' energetic offset (ΔE_{TL}) for the doped inorganic parameter set. We note that we have multiplied V_{BI} and V_{flat} by the elementary charge (q) so that they can be plotted on the same axis as $\Delta E_{F,TLs}$. This figure shows that, when the transport layers are highly conductive and have a high permittivity, V_{flat} is determined by $\Delta E_{F,TLs}$. For small values of $\Delta E_{F,TLs}$, V_{flat} falls slightly below $\Delta E_{F,TLs}$ and this is due to the presence of an injection barrier from the electrodes into the transport layers, which creates a depletion region at the transport layer/electrode interface. (b) V_{BI} and V_{flat} for the undoped organic parameter set as a function of ΔE_{TL}. Since the transport layers are intrinsic, we do not show $\Delta E_{F,TLs}$ in this case. It is apparent that the use of transport layers with low conductivity and permittivity can lead to a significant reduction in V_{flat} relative to V_{BI}, as is discussed in **Supplementary Note Three**.

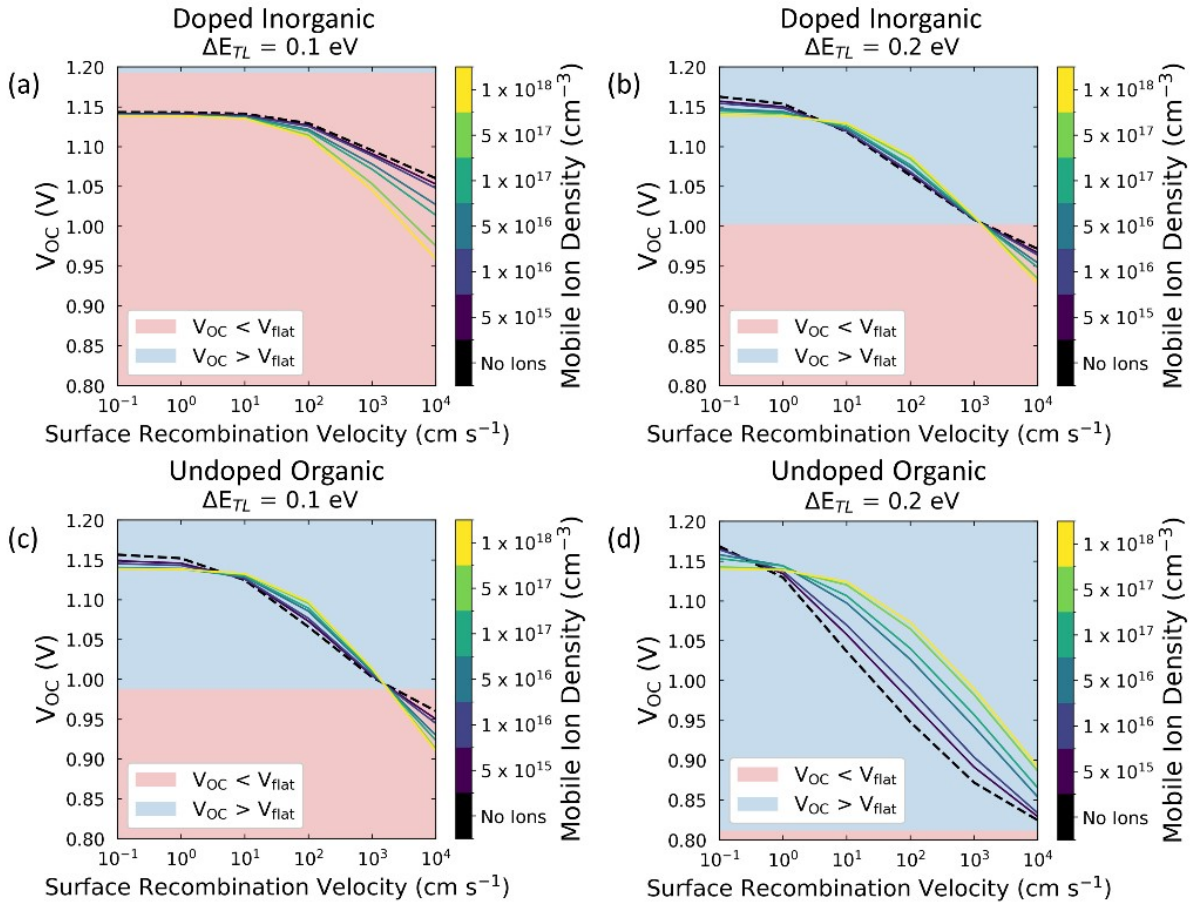

Figure S3: The effect of surface recombination velocity (v_S) on the ionic modulation of V_{OC} for different combinations of parameter set and transport layer energetic offset (ΔE_{TL}). Figures (a) and (b) show the case of doped inorganic transport layers for which the flat band condition across the perovskite (V_{flat}) is determined by the Fermi level offset between the transport layers (**Figure S2**). In (a), where there is a small ΔE_{TL}, this results in V_{OC} lying below V_{flat} for all values of v_S (in the cases of low v_S, the device becomes limited by Shockley-Read-Hall recombination). Under these conditions, the presence of mobile ions does not improve V_{OC} as the device reaches V_{OC} prior to the reversal of the electric field across the perovskite. Thus, the distribution of mobile ions always results in higher minority carrier concentrations at the perovskite/transport layer interfaces than is the case in an equivalent device without mobile ions, resulting in a higher rate of surface recombination for a given applied voltage. The situation is different in Figure (b), where ΔE_{TL} is larger thereby reducing V_{flat}. Under these circumstances, mobile ions can improve V_{OC} via the mechanism discussed in the main text for values of v_S in the range 1-1000 cms^{-1}. For values of $v_S \gtrsim 1000$ cms-1, we see that $V_{OC} < V_{flat}$ and so the presence of mobile ions reduces V_{OC}, as in Figure (a). For values of $v_S \lesssim 1$ cms^{-1}, we also observe that the inclusion of ions does not improve V_{OC}. However, in this case, it is because the recombination current becomes dominated by Shockley-Read-Hall recombination (see **Figure S4**).

Figures (c) and (d) show the case of undoped organic transport layers. This reduces V_{flat} relative to the doped inorganic case (**Figure S2**) and means that it is possible to see an improvement in V_{OC} due to mobile ions for a lower value of ΔE_{TL}, as can be seen by contrasting Figures (a) and (c). In Figure (d), V_{flat} lies below V_{OC} for all values of v_S due to the larger value of ΔE_{TL}, meaning that the presence of mobile ions always results in an increase in V_{OC} so long as surface recombination is the dominant contribution to the recombination current (which, again, is not the case for $v_S \lesssim 1$ cms^{-1}) . Additionally, it is interesting to note that Figures (b) and (c) show very similar trends in V_{OC}, despite there being a

significant difference in the properties of their transport layers. We note that the choice of ΔE_{TL} for these two figures means that they have comparable values of V_{flat}, which demonstrates how transport layer properties play a key role in determining the distribution of the electrostatic potential in a working device. Furthermore, these figures suggests that V_{OC} is largely determined by the value of V_{flat} and thus that greater consideration should be paid to the capacitive properties of transport layers used in PSCs.

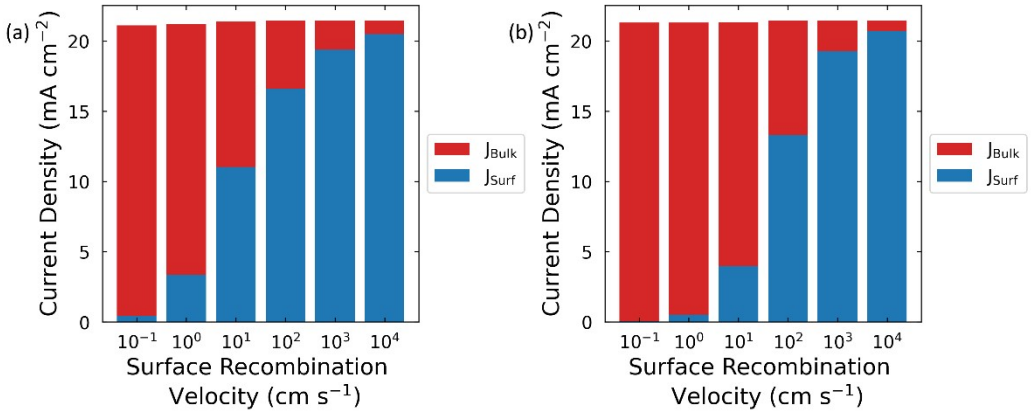

Figure S4: A breakdown of the non-radiative contributions to the recombination current at open circuit for the simulation results shown in **Figure S3b**. Figure (a) shows the case with no mobile ions and Figure (b) shows the case with a mobile ion concentration of 10^{18} cm^{-3}. Considering Figure (a), this device is dominated by surface recombination (J_{Surf}), rather than bulk recombination (J_{Bulk}) under open circuit conditions for values of $v_S > 10$ cm s^{-1}. This closely matches the point on **Figure S3b** where the devices including mobile ions start to have a higher V_{OC} than those without, demonstrating that mobile ions only lead to an increase in V_{OC} when surface recombination losses are dominant. We note here that, in a device with a longer bulk lifetime than that assumed in our simulations (100 ns), the presence of mobile ions would lead to an increase in V_{OC} for lower values of the surface recombination velocity. Turning to Figure (b), we see that, in a device with a high mobile ion concentration, the fraction of surface recombination at open circuit is lower than in the corresponding device with no ions, up to $v_S \approx$ 1000 cm s^{-1}. This is the point at which $V_{OC} < V_{flat}$, meaning that the presence of mobile ions acts to increase J_{surf}, as described in the main text.

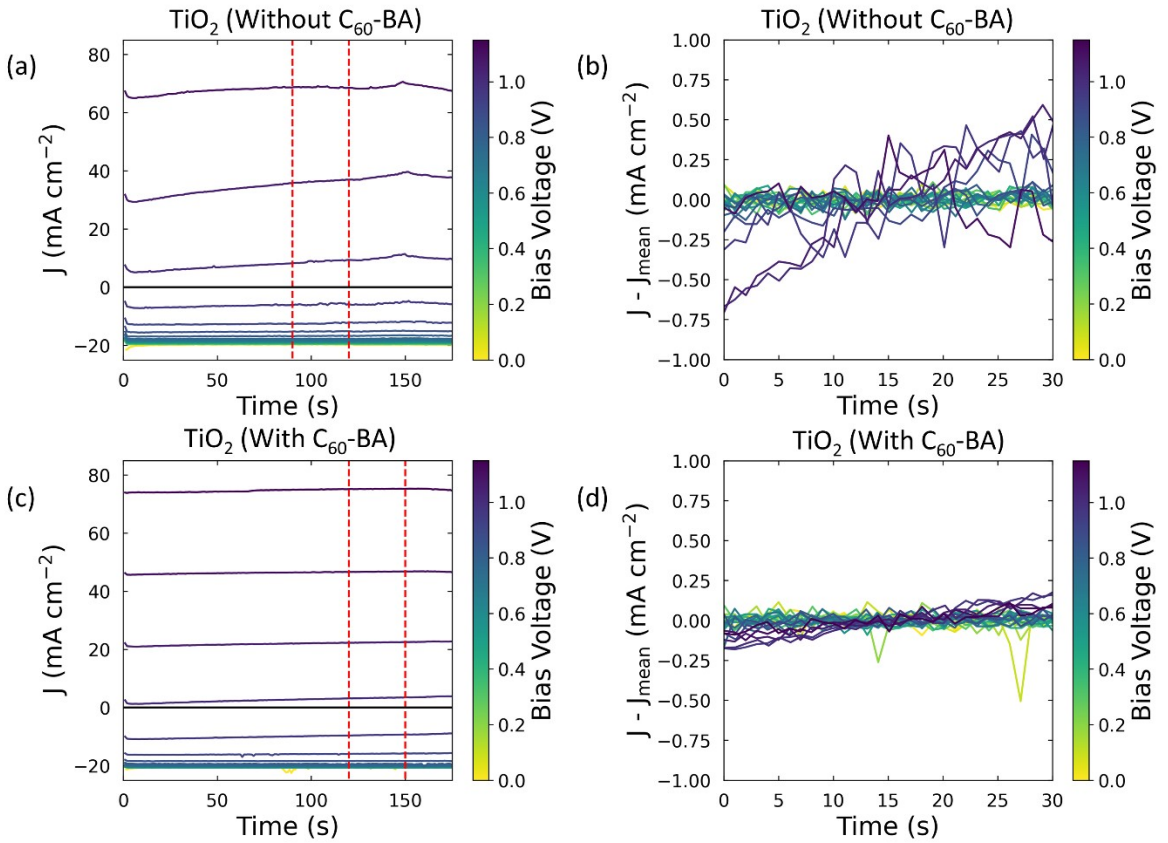

Figure S5: Current densities (*J*) measured during the stabilisation phase of the Stabilise and Pulse measurements. Figures (a-b) are for the devices without C_{60}-BA and figures (c-d) are for those with C_{60}-BA. In both cases, the first column shows all the data measured over the entire stabilisation period, and the vertical red lines indicate the thirty second time span over which *J* was averaged to extract the current values for the QSS JVs. The second column focuses on these thirty seconds and shows the difference between the measured current and its mean value over this time window. It is clear that the current is less stable at higher bias voltages, though the C_{60}-BA layer seems to improve the device stability (see also **Figure S18**). This suggests that the observed change in *J* at longer times is linked to processes which occur at the perovskite/TiO_2 interface, rather than the movement of mobile ionic charge.

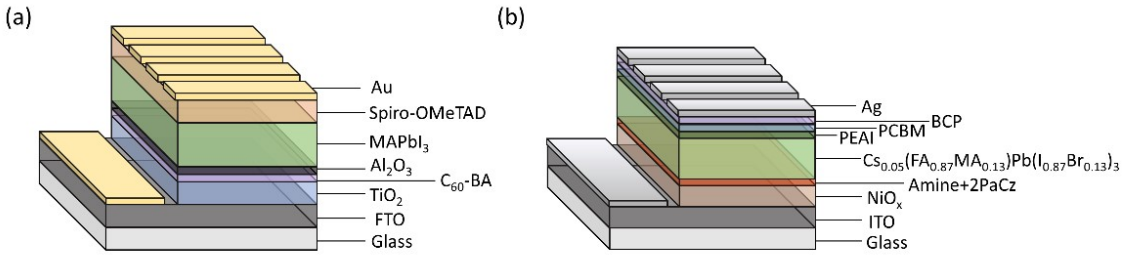

Figure S6: Device stacks for (a) the n-i-p $MAPbI_3$ devices used to measure the results shown in **Figure 2** of the main text and (b) the p-i-n triple cation device used to measure the results shown in **Figure 3** of the main text.

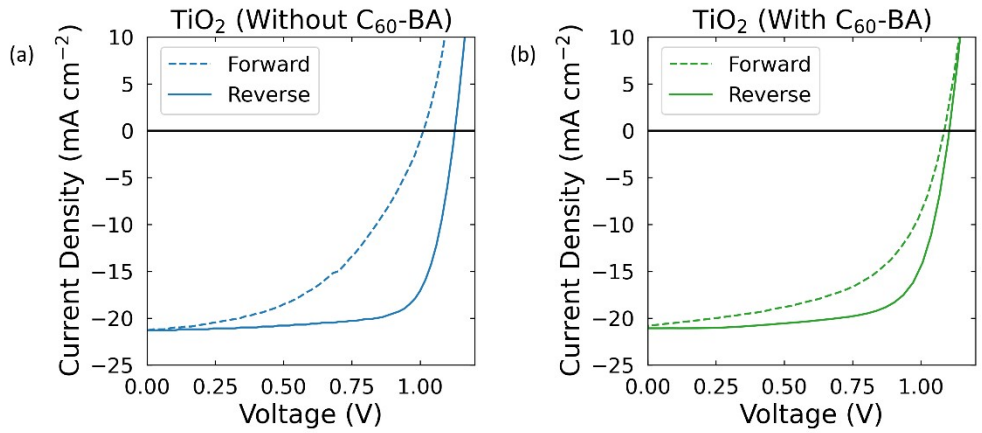

Figure S7: JV curves measured under the Solar Sim using the protocol described in the **Methods** for (a) the Au/Spiro-OMeTAD/MAPI/TiO_2/FTO device stack and (b) the Au/Spiro-OMeTAD/MAPI/C_{60}-BA/TiO_2/FTO device stack. JV parameters are given in **Table S3** and **Table S4**, respectively.

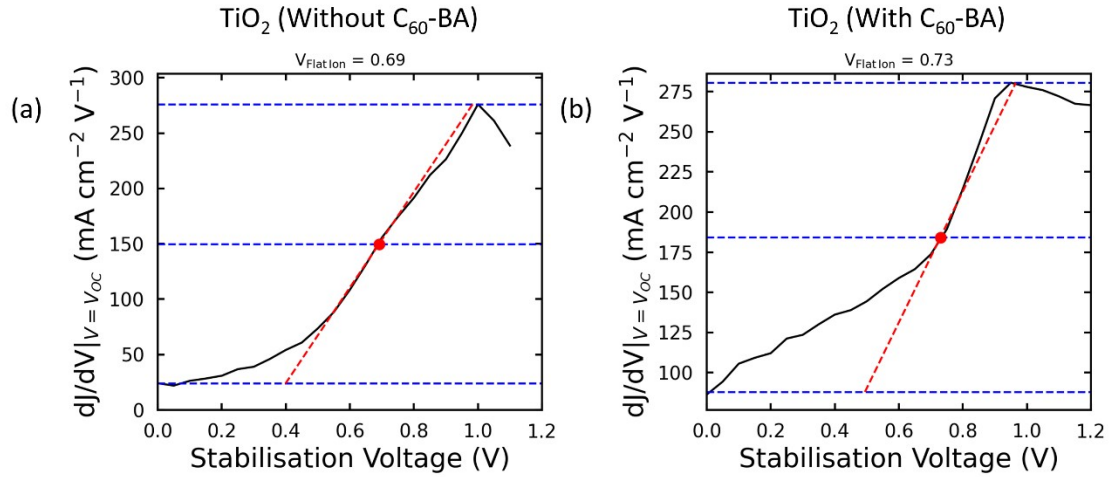

Figure S8: Plots used to extract the value of V_{flat} from the Stabilise and Pulse data for (a) the device without C_{60}-BA and (b) the device with C_{60}-BA. Details of the fitting procedure are given in the **Methods** section.

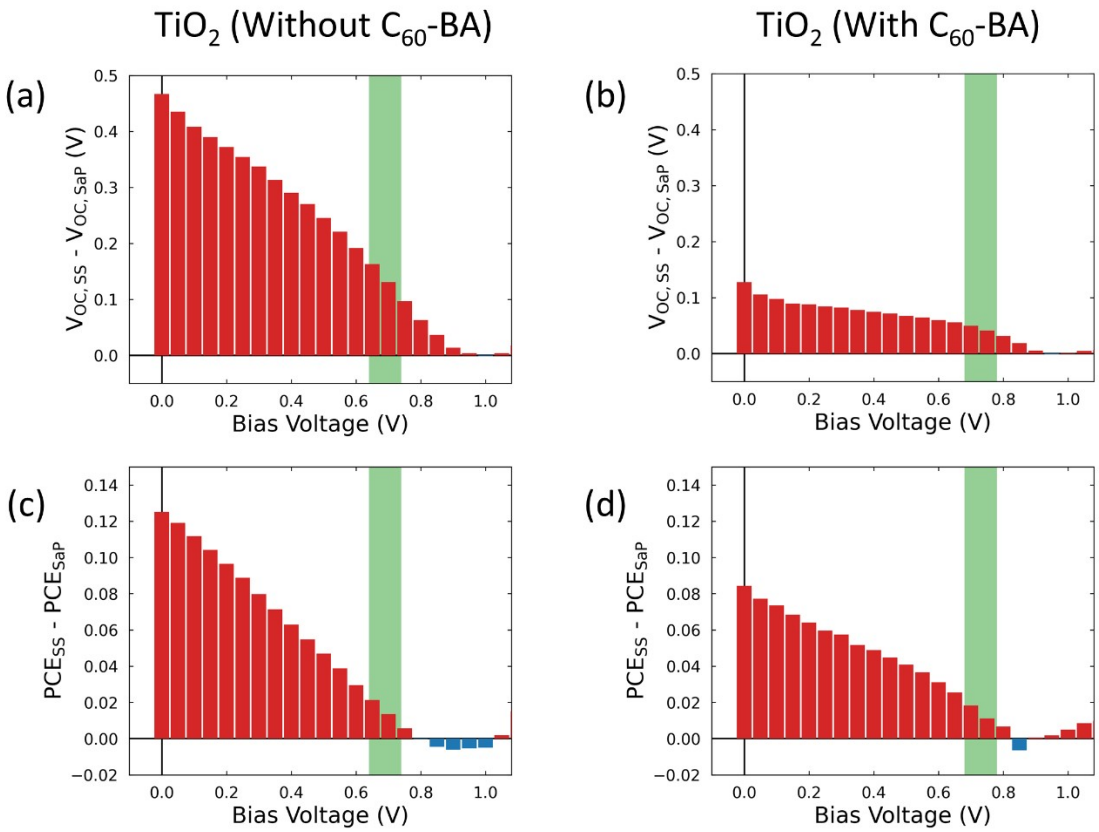

Figure S9: Difference between (a-b) V_{OC} and (c-d) PCE as measured from the JVs with the ions at quasi-steady state and the JVs as measured using the Stabilise and Pulse (SaP) technique at different bias voltages. The left-hand column shows the device without C_{60}-BA and the right-hand column shows the device with C_{60}-BA. In all cases, the green shaded region indicates the value extracted for V_{flat} (see **Methods** and **Figure S8**) with the associated error (±0.05 V).

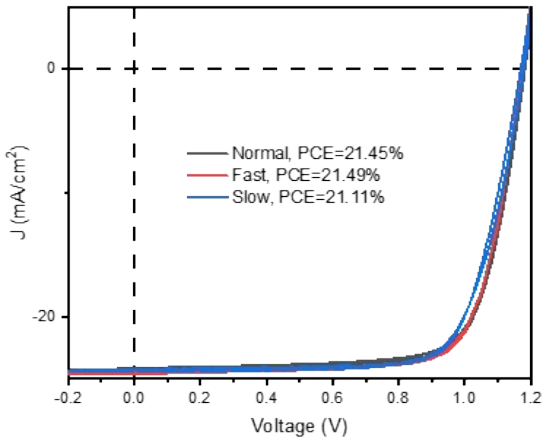

Scan Speed	Direction	V_{OC} (V)	J_{SC} (mA cm^{-2})	PCE (%)	FF
Normal	Reverse	1.17	24.00	21.45	0.76
	Forward	1.19	24.00	21.13	0.73
Fast	Reverse	1.15	24.58	21.49	0.76
	Forward	1.15	24.58	21.59	0.76
Slow	Reverse	1.18	24.33	20.90	0.73
	Forward	1.17	24.33	21.11	0.74

Figure S10: JV scans of the ITO/NiO_x/Amine/2PaCz/perovskite/PEAI/PCBM/BCP/Ag device shown in **Figure 3** of the main text. The perovskite composition is $Cs_{0.05}(FA_{0.87}MA_{0.13})Pb(I_{0.87}Br_{0.13})_3$ and the full device stack is shown in **Figure S6**. JV parameters are provided in the table and see the **Methods** for a description of the measurement protocol used to measure the JV scans.

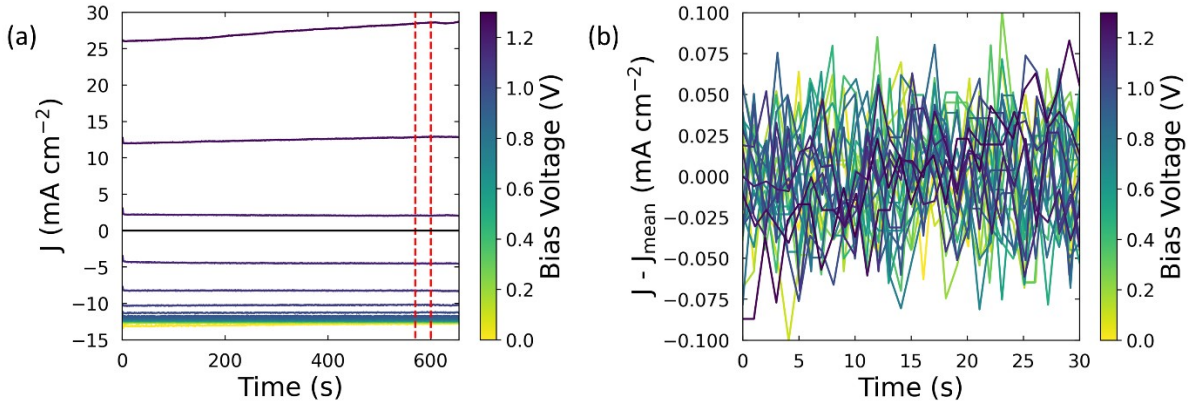

Figure S11: Stabilisation data for the Stabilise and Pulse measurement shown in **Figure 4** of the main text. (a) Current density (J) measured during the stabilisation phase of the Stabilise and Pulse measurements for all measured values of V_{bias}. The vertical red lines indicate the thirty second time span over which J was averaged to extract the current values for the quasi-steady state (QSS) JVs. (b) The current measured in the thirty second time period indicated in (a) minus its mean value.

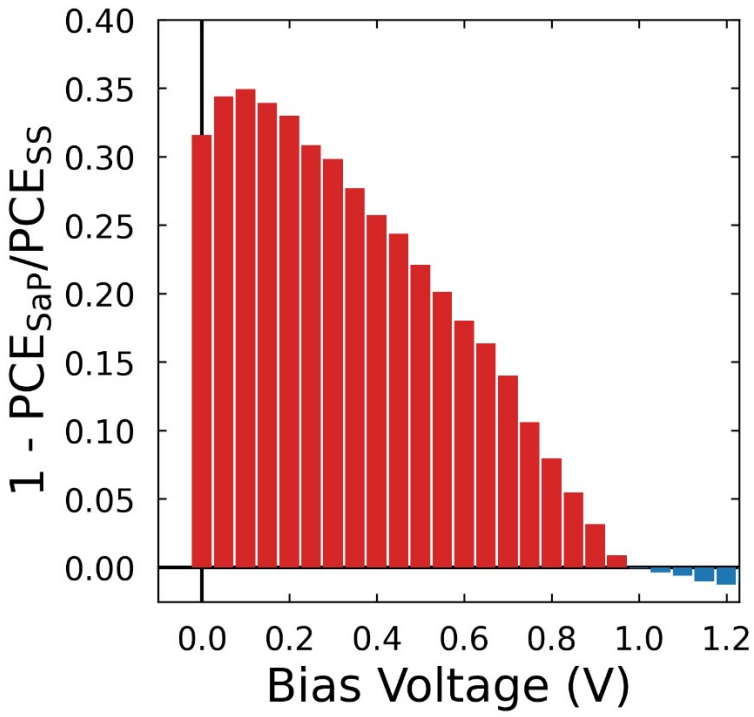

Figure S12: The normalised difference between the PCE of the JV curve where the ions remain at quasi-steady state (PCE_{SS}) and those measured using the Stabilise and Pulse protocol at different values of V_{bias} (PCE_{SaP}). We have normalised this data as, for measurements on devices using the triple cation perovskite composition, the intensity of the LED light was calibrated such that the device gave half the J_{SC} value as measured under the Solar Simulator (see main text). However, we did not explicitly measure this intensity and so cannot accurately convert our data to a PCE. Regardless, this plot indicates that mobile ions improve the device's PCE if $V_{flat} < 1.0$ V. Our simulation results indicate that $V_{flat} \approx 0.85$ eV, corresponding to a PCE improvement of ~ 1% due to mobile ions if we assume an intensity of 50 mWcm^{-2}.

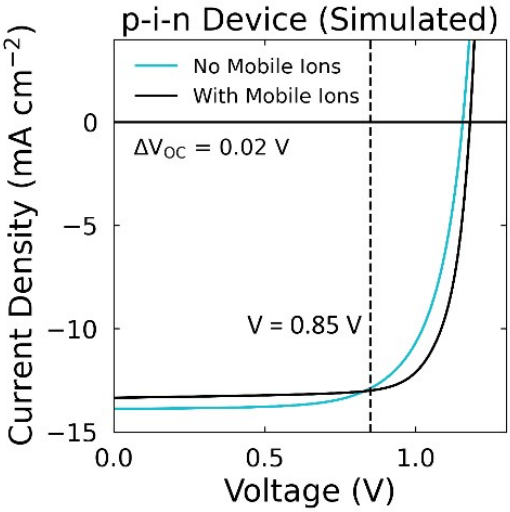

Figure S13: Simulated JV curves obtained using the parameters listed in **Table S5** with and without the inclusion of a mobile ionic species. The black dashed line indicates V = 0.85 V which is the voltage at which the 'No Mobile Ions' and 'With Mobile Ions' JV curves intersect. As commented upon in the caption to **Figure S1**, this intersection occurs at V_{flat}, thereby demonstrating that V_{flat} = 0.85 V for this device.

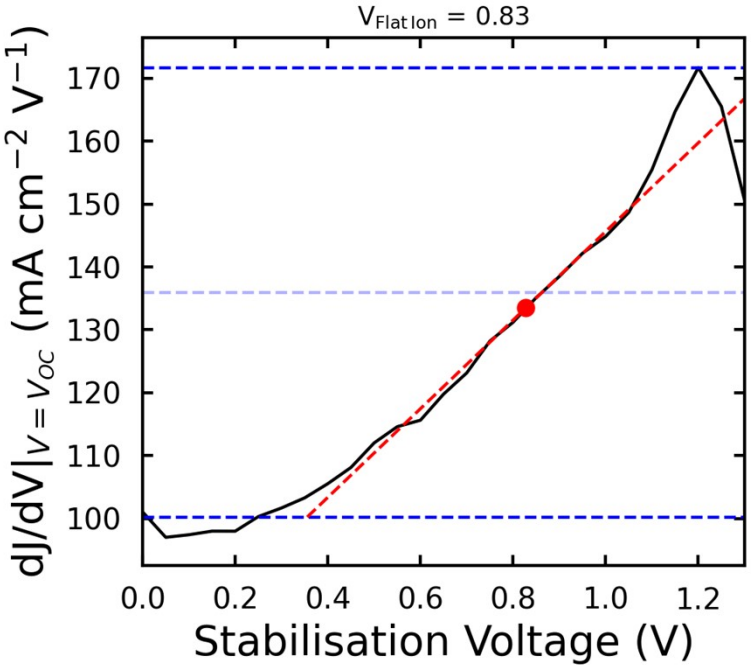

Figure S14: Plot used to extract the value of V_{flat} from the Stabilise and Pulse data for the p-i-n device shown in **Figure 4a** of the main text. Details of the fitting procedure are given in the **Methods** section.

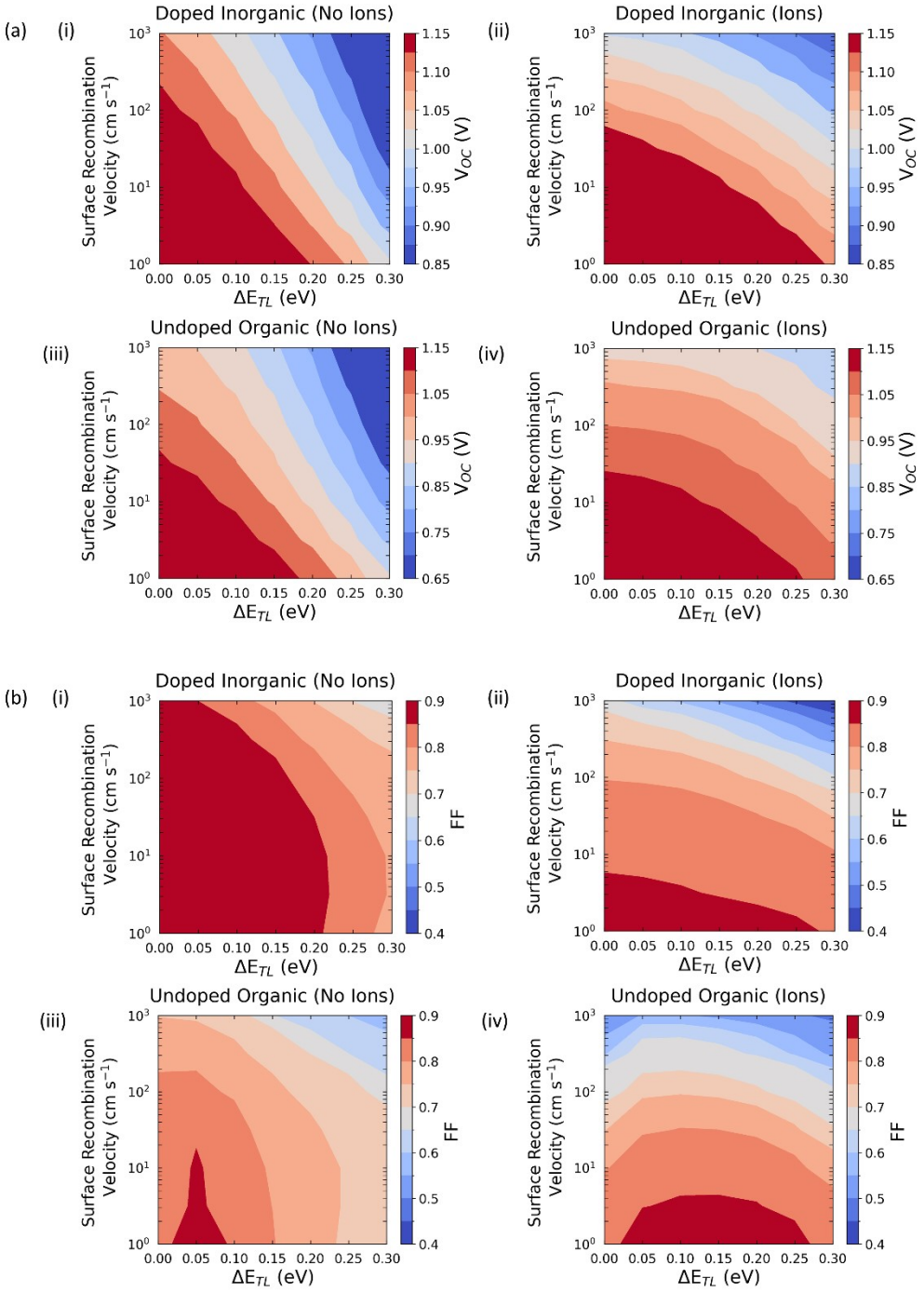
(a)
(i)
Doped Inorganic (No Ions)
(ii)
Doped Inorganic (Ions)
(iii)
Undoped Organic (No Ions)
(iv)
Undoped Organic (Ions)
Surface Recombination Velocity (cm s^{-1})
ΔE_{TL} (eV)
V_{OC} (V)
(b)
(i)
Doped Inorganic (No Ions)
(ii)
Doped Inorganic (Ions)
(iii)
Undoped Organic (No Ions)
(iv)
Undoped Organic (Ions)
Surface Recombination Velocity (cm s^{-1})
ΔE_{TL} (eV)
FF

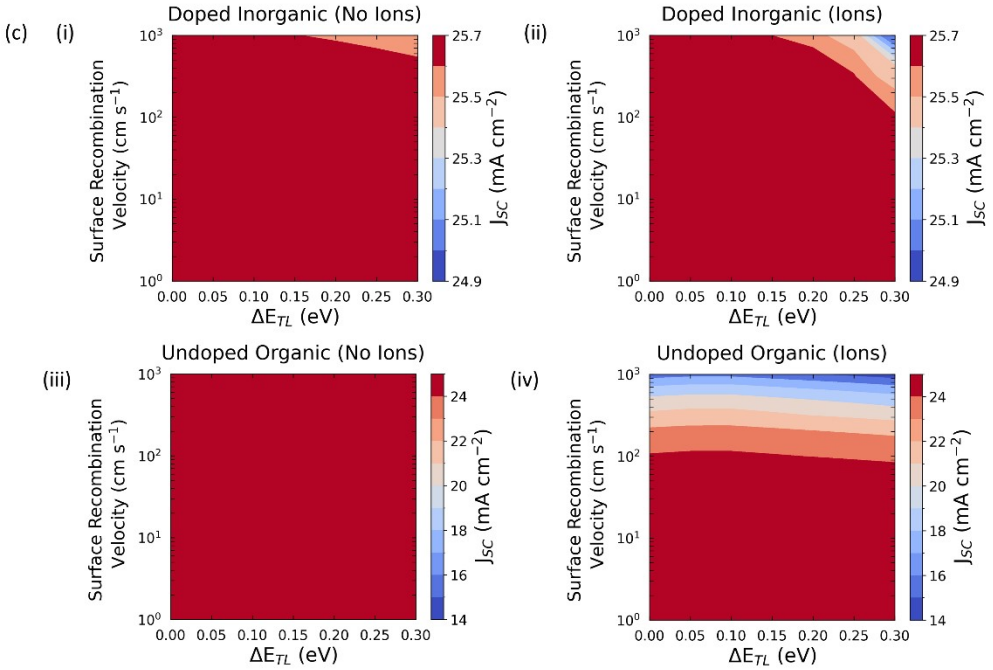

Figure S15: (a) V_{OC} (b) fill factor (FF) and (c) short-circuit current density (J_{SC}) of simulated devices shown in **Figure 4** as a function of surface recombination velocity and ΔE_{TL} for (i-ii) the doped inorganic parameter set without (left-hand column) and with (right-hand column) the inclusion of mobile ions and (iii-iv) the undoped organic parameter set without (left-hand column) and with (right-hand column) the inclusion of mobile ions. When mobile ions were included, we used a mobile ion concentration of 10^{18} cm^{-3}. By comparing the two columns, we can see that the inclusion of mobile ions in the simulations reduces the dependence of V_{OC} and FF on ΔE_{TL}, and that this effect is particularly pronounced for the undoped organic parameter set. However, each of J_{SC}, FF and V_{OC} become more sensitive to increases in the surface recombination velocity when mobile ions are present.

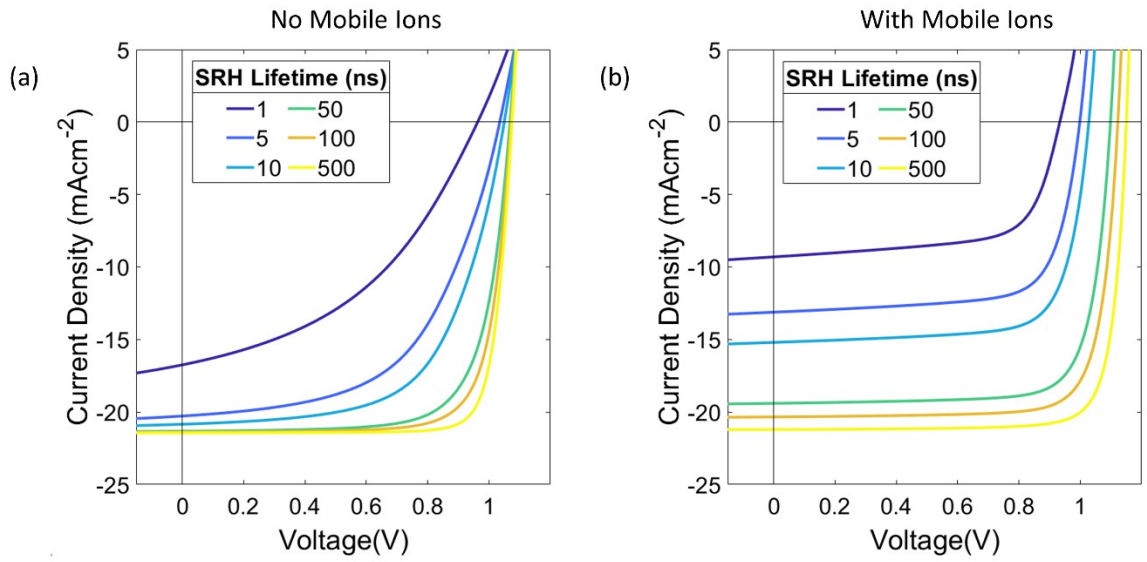

Figure S16: The dependence of JV curves on bulk Shockley-Read-Hall (SRH) lifetime for the doped inorganic parameter set with a fixed energetic offset of 0.25 eV and (a) no mobile ions and (b) a mobile ion density of 10^{18} cm^{-3}. The case with mobile ions was simulated such that the ions remained at quasi-steady state. The trap states were assumed to lie midgap in the perovskite and electrons and holes were given the same SRH lifetime. The presence of mobile ions increases the loss in photocurrent at low bias voltages, but this device maintains a high fill factor since field screening by the mobile ionic species reduces the dependence of extraction efficiency on the applied bias.

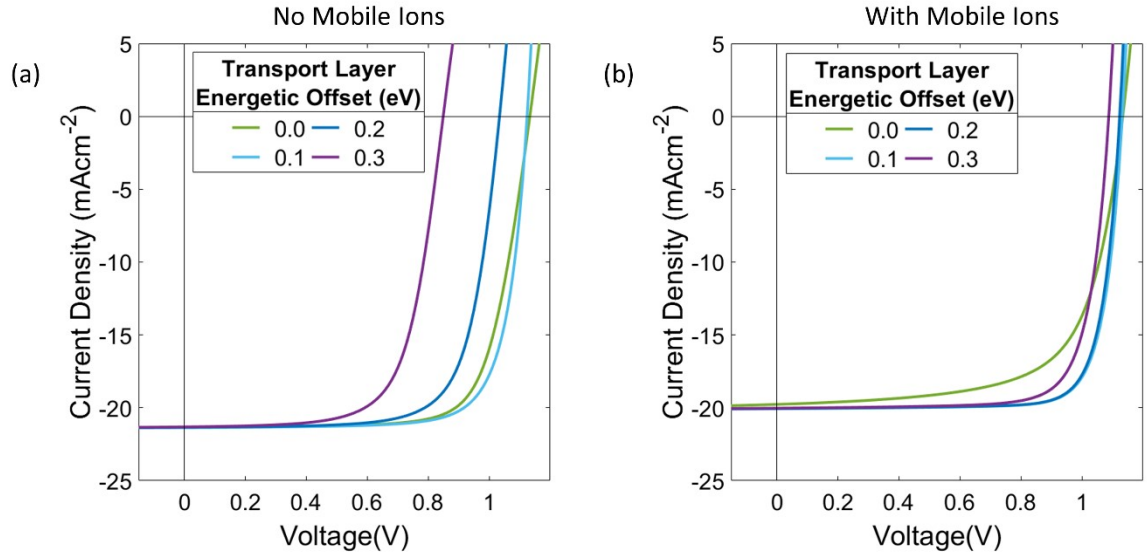

Figure S17: The dependence of JV curves on transport layer energetic offset (varied symmetrically) for the undoped organic parameter set with (a) no mobile ions and (b) a mobile ion density of 10^{18} cm^{-3}. The case with mobile ions was simulated such that the ions remained at quasi-steady state. In both devices, the fill factor improves upon increasing the energetic offset from 0.0 eV to 0.1 eV, but the improvement is greater in the case with mobile ions. Additionally, this figure illustrates how V_{OC} is far less sensitive to transport layer energetic offsets in devices with a mobile ionic species (subject to the caveats discussed in the main text and **Figure S3**).

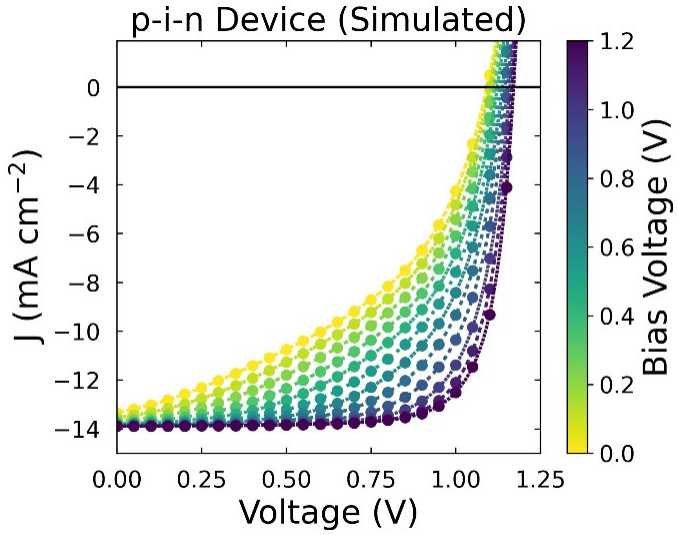

Figure S18: Figure to show that the two protocols which are described in the **Methods** section and used to simulate the Stabilise and Pulse measurements yield equivalent results. The solid circles show the results of the explicit simulations of the Stabilise and Pulse procedure, whereas the dashed lines show the results of JV scans performed with the ion mobility set to zero following a prebiasing period at the desired bias voltage. It can be seen that both simulation protocols yield equivalent results, but the JV scans allow for a higher voltage resolution along the *x*-axis.

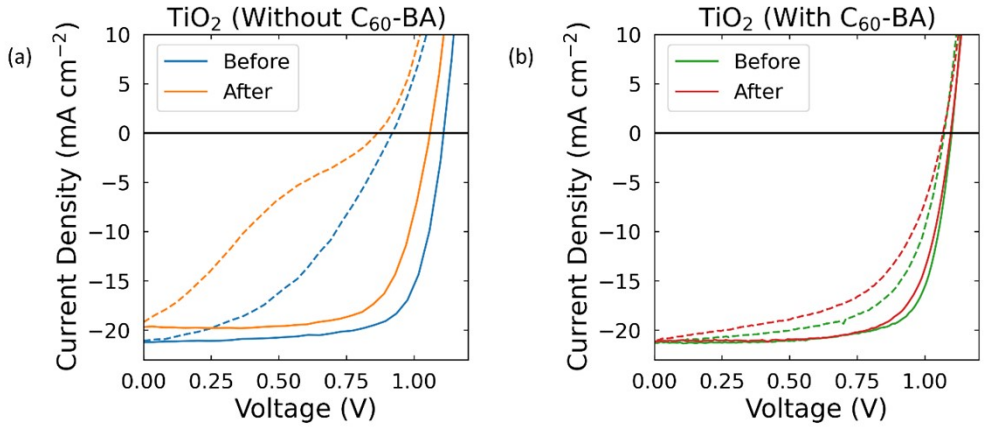

Figure S19: JV curves before and after the Stabilise and Pulse measurement for the devices shown in **Figure 2** of the main text. Solid lines indicate the reverse scan, and dashed lines the forward scan. We note that these JV scans were not performed under the Solar Sim, but under the LED illumination of the Stabilise and Pulse set-up, which is why the JV curves measured before the Stabilise and Pulse measurement do not perfectly match those shown in **Figure S6**. The device without the C_{60}-BA interlayer shows greater degradation after the measurement, which we believe is linked to the instability in the device's current which was observed at high values of V_{bias} (see **Figure S4**).

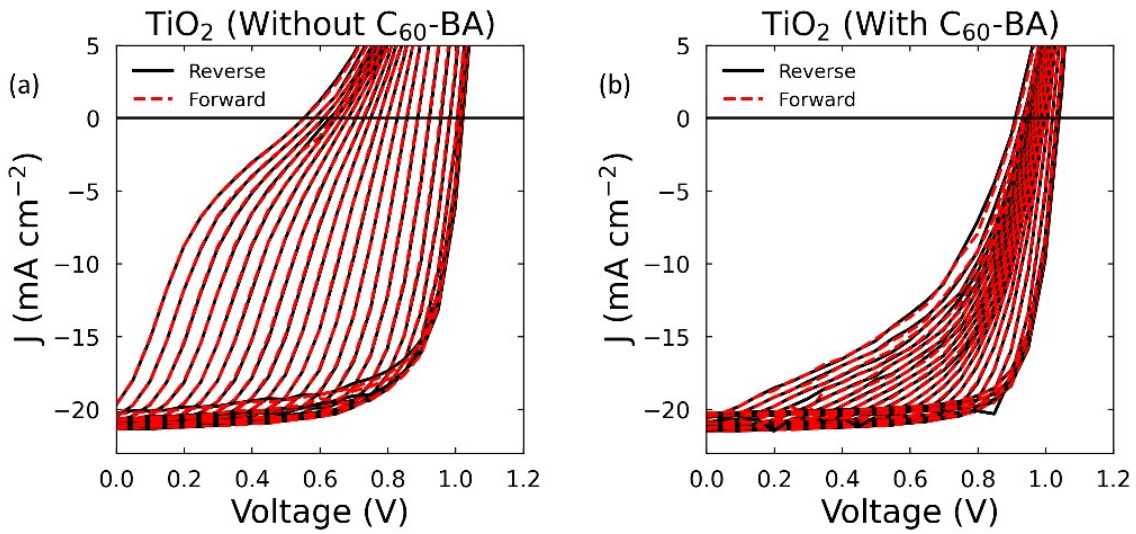

Figure S20: The Stabilise and Pulse data shown in **Figures 2a-b** of the main text for the TiO2 device (a) without and (b) with C_{60}-BA. Here, we have shown the forward and reverse JV scans in contrasting colours to illustrate the lack of hysteresis during the Stabilise and Pulse measurement.

Supplementary Tables

Table S1: Summary of the simulation parameters for the transport layers. When not otherwise stated, the same parameters were used for the electron and hole transport layers (ETL and HTL, respectively). Recombination parameters (Shockley-Read Hall Lifetimes and radiative recombination rate) were set such that there were no recombination losses within the transport layers, except recombination at interfaces with the perovskite and electrode. E_C and E_V refer to the conduction and valance band energies, respectively.

Parameter	Doped Inorganic	Undoped Organic
Bandgap	2.50 eV	2.50 eV
ETL Fermi Level	E_C – 0.1 eV	Midgap
HTL Fermi Level	E_V + 0.1 eV	Midgap
Energy Level of Trap States	Midgap	Midgap
Thickness	100 nm	20 nm
Carrier Mobility	10 $cm^2 V^{-1} s^{-1}$	0.001 $cm^2 V^{-1} s^{-1}$
Relative Permittivity	50	3.5
Effective Density of States	5×10^{18} cm^{-3}	1×10^{20} cm^{-3}

Table S2: Summary of the simulation parameters for the perovskite layer which were used to generate the results shown in **Figure 1** of the main text. Monomolecular trap states were assumed to lie in the middle of the bandgap and the perovskite was treated as an intrinsic semiconductor. At the interfaces, trap states were placed midgap for the perovskite layer and thus surface recombination velocities were assumed to be equal for electrons and holes.

Parameter	Value	Ref
Perovskite Bandgap	1.60 eV	1
Perovskite Valance Band Energy	-5.4 eV	2
Perovskite Thickness	400 nm	a
Perovskite Carrier Mobility	1.0 $cm^2 V^{-1} s^{-1}$	3
Shockley-Read-Hall Lifetime	100 ns	4
Radiative Recombination Rate	5×10^{-11} $cm^{-3} s^{-1}$	5
Perovskite Relative Permittivity	25	6
Perovskite Effective Density of States	5×10^{18} cm^{-3}	7

a) Typical thickness for perovskite layer.

To simulate the contour plots shown in **Figure 4** of the main text we changed the perovskite bandgap and Shockley-Read-Hall lifetime to match the values given in **Ref. 2** of the main text which used $FAPbI_3$ for the perovskite layer, as opposed to $MAPbI_3$. This meant that we reduced the bandgap to 1.50 eV (while maintaining an intrinsic perovskite layer with midgap trap states) and we increased the Shockley-Read-Hall lifetime to 3 μs. Additionally, as we could not obtain n and k values for $FAPbI_3$, simulations were done at 1.2 Suns to match the J_{SC} values reported in **Ref. 2**. All other simulation parameters remained as reported in **Tables S1-2**.

As noted in the main text, the built in potential across the device was held at 1.1 V and we used symmetric energetic offsets between the electrode work function and the relevant band edge of the transport layers. However, for transport layer-perovskite energetic offsets > 0.15 eV, it was not possible to maintain V_{BI} at 1.1 V as this would have caused the electrode's work function to lie within the conduction (valance) band of the ETL (HTL). In these cases, the work functions were reduced such that they always lay 0.1 eV below the relevant band edge. This ensured an Ohmic contact between the electrodes and the transport layers in the case of the doped inorganic parameter set.

In simulations where the surface recombination velocity was not varied, we used a default value of 10 cm s^{-1}, as this value allowed us to access regimes dominated by either SRH recombination or surface recombination within the range of ΔE_{TL} values investigated in this work.

Table S3: Summary of the JV parameters for the Au/Spiro-OMeTAD/$MAPbI_3$/TiO_2/FTO devices discussed in the main text. JV parameters are given for three cases: as measured under the Solar Simulator using the protocol described in the **Methods** section (parameters taken from the reverse scan), as measured with the mobile ions at quasi-steady state (QSS JV) and as measured using Stabilise and Pulse measurements carried out at $V_{bias} = V_{flat}$ (SaP JV). The parameters corresponding to the devices shown in the main text are given in bold and data for all other devices is shown in **Supplementary Note Six**. Additionally, we provide the value of V_{flat} extracted from our analysis of the Stabilise and Pulse data in column 2.

Device Number	V_{flat} (V)	Method	J_{SC} (mA cm^{-2})	V_{OC} (V)	FF	PCE (%)
1	**0.69 ± 0.05**	**Solar Sim**	**21.30**	**1.127**	**0.75**	**17.90**
		QSS JV	**19.72**	**1.019**	**0.71**	**14.26**
		SaP JV	**21.34**	**0.856**	**0.66**	**12.13**
2	0.66 ± 0.05	Solar Sim	20.78	1.081	0.71	16.00
		QSS JV	18.60	0.989	0.64	11.75
		SaP JV	21.49	0.827	0.61	10.80
3	0.64 ± 0.05	Solar Sim	21.89	1.080	0.70	16.47
		QSS JV	20.45	1.005	0.62	12.81
		SaP JV	22.79	0.823	0.62	11.64
4	0.67 ± 0.05	Solar Sim	21.82	1.082	0.71	16.68
		QSS JV	18.98	1.008	0.60	11.47
		SaP JV	21.30	0.855	0.62	11.38
5	0.65 ± 0.05	Solar Sim	20.25	1.073	0.69	15.01
		QSS JV	18.59	0.991	0.61	11.19
		SaP JV	21.44	0.846	0.57	10.34

Table S4: Summary of the JV parameters for the Au/Spiro-OMeTAD/MAPI/C_{60}-BA/TiO_2/FTO devices discussed in the main text. The parameters corresponding to the devices shown in the main text are given in bold and data for all other devices is shown in **Supplementary Note Six**. For further details, see the caption of **Table S3**.

Device Number	V_{flat} (V)	Method	J_{SC} (mA cm^{-2})	V_{OC} (V)	FF	PCE (%)
1	0.76 ± 0.05	SolarSim	21.08	1.104	0.71	16.55
		QSS JV	19.89	1.027	0.79	16.10
		SaP JV	21.88	0.987	0.68	14.78
2	0.75 ± 0.05	SolarSim	21.24	1.081	0.73	16.69
		QSS JV	20.25	0.997	0.67	13.48
		SaP JV	21.41	0.973	0.63	13.04
3	0.72 ± 0.05	SolarSim	21.70	1.074	0.74	17.24
		QSS JV	21.10	1.005	0.72	15.32
		SaP JV	21.79	0.970	0.67	14.17
4	0.70 ± 0.05	SolarSim	20.34	1.078	0.71	15.67
		QSS JV	19.85	1.006	0.74	14.75
		SaP JV	20.22	0.980	0.70	13.95
5	**0.73 ± 0.05**	**SolarSim**	**21.30**	**1.099**	**0.74**	**17.34**
		QSS JV	**20.68**	**1.037**	**0.77**	**16.55**
		SaP JV	**21.45**	**0.996**	**0.72**	**15.46**
6	0.74 ± 0.05	SolarSim	21.85	1.068	0.73	17.09
		QSS JV	20.73	0.986	0.64	13.16
		SaP JV	22.04	0.937	0.64	13.18

Table S5: Parameters set used to simulate the Stabilise and Pulse measurements performed on the high-performance p-i-n device, the results of which are shown in **Figure 3c** of the main text. The perovskite was assumed to be intrinsic and trap states (both bulk and interfacial) were assumed to lie midgap. Where no comment or reference is given, parameters were tuned to qualitatively reproduce the behaviour observed in the Stabilise and Pulse measurements. We have assumed that the dominant effect of the interfacial PEAI and 2PACz layers (see device stack shown in **Figure S6**) is to reduce surface recombination, thereby motivating our use of low values for these parameters. Measurements were simulated under 0.65 suns so as to match the experimentally measured J_{SC} values.

Parameter	Value	Ref
Perovskite Bandgap	1.60 eV	[8]
Perovskite Valance Band Energy	-5.5 eV	[8]
Perovskite Thickness	400 nm	a
Perovskite Carrier Mobility	0.25 $cm^2 V^{-1} s^{-1}$	[3]
Shockley-Read-Hall Lifetime	400 ns	-
Radiative Recombination Rate	5×10^{-11} $cm^{-3} s^{-1}$	[5]
Perovskite Relative Permittivity	25	[6]
Perovskite Effective Density of States	5×10^{18} cm^{-3}	[7]
Perovskite Mobile Ion Density	7×10^{16} cm^{-3}	[6]
ETL Bandgap	2.00 eV	[9]
ETL Conduction Band Energy	-4.1 eV	b
ETL Fermi Level	-5.1 eV	c
ETL Thickness	25 nm	d
ETL Carrier Mobility	0.005 $cm^2 V^{-1} s^{-1}$	[10]
ETL Relative Permittivity	3.5	e
ETL Effective Density of States	1×10^{20} cm^{-3}	[11]
Surface Recombination Velocity of Holes at the Perovskite/ETL Interface	0.65 cms^{-1}	-
Surface Recombination Velocity of Electrons at the Perovskite/ETL Interface	10^7 cms^{-1}	f
Cathode Work Function	-4.175 V	-
HTL Bandgap	3.00 eV	g
HTL Valance Band Energy	-5.3 eV	h
HTL Fermi Level	-5.1 eV	[12]
HTL Thickness	80 nm	[12]

HTL Carrier Mobility	0.01 $cm^2 V^{-1} s^{-1}$	[13]
HTL Relative Permittivity	12	[14]
HTL Effective Density of States	1 x 10^{19} cm^{-3}	i
Surface Recombination Velocity at the of Electrons Perovskite/HTL Interface	0.1 cms^{-1}	-
Surface Recombination Velocity at the of Holes Perovskite/HTL Interface	10^7 cms^{-1}	-
Anode Work Function	-5.225 V	-

a) Typical thickness for perovskite layer.
b) Values in the range -4.2 eV to -3.9 eV have been reported for PCBM.[9,15] We chose the value in this range which best reproduced the Stabilise and Pulse measurements.
c) PCBM was assumed to be an intrinsic semiconductor.
d) Typical thickness for undoped organic ETLs.
e) Typical value for organic semiconductors.
f) Setting a high value for the majority carrier surface recombination velocity was observed to have a negligible effect on simulated JV curves with the ions at quasi-steady state. However, this parameter had a large effect on the shape of the simulated Stabilise and Pulse curves at low bias voltages. Thus, it's value was varied to match the experimental results, with larger values found to lead to less 's-shaped' JV curves at low bias voltages.
g) Bandgap of NiO_x varies depending on fabrication route, but typically > 3.0 eV. Further increases in the band gap yielded no change in the simulation results, but increased the time taken per simulation and so this parameter was set to 3 eV.
h) Values in the range -5.45 eV to -5.05 eV have been reported for NiO.[12,16] We chose the value in this range which best reproduced the Stabilise and Pulse measurements.
i) Calculated using parabolic band approximation and $m^* = m_e$.[17]

Table S6: Parameter set used to simulate the Stabilise and Pulse measurements performed on the Au/Spiro-OMeTAD/$MAPbI_3$/C_{60}-BA/TiO_2/FTO device stacks, the results of which are shown in **Supplementary Note Four**. In these simulations, the $MAPbI_3$ was assumed to be intrinsic and trap states (both bulk and interfacial) were assumed to lie midgap. Where no comment or reference is given, parameters were tuned to qualitatively reproduce the behaviour observed in the Stabilise and Pulse measurements.

Parameter	Value	Ref
Perovskite Bandgap	1.60 eV	[1]
Perovskite Valance Band Energy	-5.4 eV	[2]
Perovskite Thickness	400 nm	a
Perovskite Carrier Mobility	3 $cm^2 V^{-1} s^{-1}$	[18]
Shockley-Read-Hall Lifetime	25 ns	-
Radiative Recombination Rate	5 x 10^{-11} $cm^{-3} s^{-1}$	[5]
Perovskite Relative Permittivity	25	[6]
Perovskite Effective Density of States	5 x 10^{18} cm^{-3}	[7]
Perovskite Mobile Ion Density	1 x 10^{17} cm^{-3}	-
ETL Bandgap	3.00 eV	b
ETL Conduction Band Energy	-4.0 eV	c
ETL Fermi Level	-4.2 eV	-
ETL Thickness	25 nm	[19]
ETL Carrier Mobility	0.1 $cm^2 V^{-1} s^{-1}$	d
ETL Relative Permittivity	19	e
ETL Effective Density of States	1 x 10^{19} cm^{-3}	f
Surface Recombination Velocity of Holes at the Perovskite/ETL Interface	50 cms^{-1} (without C_{60}-BA) 0.05 cms^{-1} (with C_{60}-BA)	-
Surface Recombination Velocity of Electrons at the Perovskite/ETL Interface	1000 cms^{-1}	g
Cathode Work Function	-4.2 V	-
HTL Bandgap	3.00 eV	h
HTL Valance Band Energy	-5.05 eV	i
HTL Fermi Level	-4.85 eV	j
HTL Thickness	200 nm	[20]
HTL Carrier Mobility	0.01 $cm^2 V^{-1} s^{-1}$	j

HTL Relative Permittivity	3.5	k
HTL Effective Density of States	1 x 10^{20} cm^{-3}	l
Surface Recombination Velocity of Electrons at the Perovskite/HTL Interface	10 cms^{-1}	-
Surface Recombination Velocity of Holes at the Perovskite/HTL Interface	1000 cms^{-1}	g
Anode Work Function	-4.85 V	-

a) Typical thickness for perovskite layer.
b) Bandgap of TiO_2 varies depending on its phase, but is typically > 3.0 eV.[21] Further increases in the band gap yielded no change in the simulation results.
c) Values in the range -4.0 eV to -4.3 eV have been reported for TiO_2.[22,23] We chose the value in this range could best account for the JV data and the Stabilise and Pulse measurements.
d) The mobility of electrons in TiO_2 varies depending upon both the phase and crystallinity of the material.[24] We have used 0.1 $cm^2V^{-1}s^{-1}$ as a conservative estimate from the values found in the literature.
e) The relative permittivity of TiO_2 depends upon both its phase and orientation. For films prepared using the sol-gel method, values in the range 19-64 have been recorded, depending upon the annealing temperature.[25] We have used 19 as this film was annealed at the temperature most similar to ours.
f) The effective mass of electrons in TiO_2 varies dramatically between different phases.[26] As the structure of the TiO_2 was unknown for these devices, we have assumed $m^* \approx m_e$ and calculated the density of states expected in the parabolic band approximation for this value of m^*. An under (over) estimate of this parameter would results in an over (under) estimate of the surface recombination velocity at the perovskite/TiO_2 interface as the rate of interfacial recombination increases as the density of states in the transport layer increases.
g) The majority carrier surface recombination velocity was observed to have a large effect on the shape of the simulated Stabilise and Pulse curves at low bias voltages. Thus, it's value was varied to match the experimental results, with larger values found to lead to less 's-shaped' JV curves at low bias voltages.
h) Value calculated from the supplier webpage is 3.16 eV. However, this parameter was set to 3 eV as further increases in the band gap yielded no change in the simulation results, but increased the time taken per simulation.
i) Values in range of -5.0 eV to -5.2 eV have been reported for Spiro-OMeTAD.[20,27] We chose the value in this range could best account for the JV data and the Stabilise and Pulse measurements.
j) Values chosen to yield a conductivity of ~7×10^{-5} Scm^{-1}, within the range of values found for Spiro-OMeTAD samples doped in a similar manner to those in this work.[28]
k) Typical value for organic semiconductors.
l) No value could be found in the literature for Spiro-OMeTAD so we have used 10^{20} cm^{-3} as this lies within the range of values commonly found for organic semiconductors.[11]

Supplementary Notes

Supplementary Note One

In this Supplementary Note, we demonstrate that our results concerning the ionic modulation of V_{OC} are still valid if there are two mobile ionic species in the perovskite. To do this, we repeated the simulations shown in **Figures 1b-c** while including a second, negatively charged ionic species. We considered two extreme cases: one in which the cation density was fixed at 10^{18} cm^{-3} and the anion density varied (**Figures S21a-b**) and the other in which we varied the density of both ionic species while assuming that the cation and anion densities were equal (**Figures S21c-d**). These figures demonstrate that the presence of a second ionic species does not affect the trends in V_{OC} which we describe in the main text. Furthermore, **Figures S21 a-b** demonstrate that, in the case where the density of one ionic species far exceeds the other, the species with the lower density has a negligible impact on the steady-state V_{OC} of the device.

To perform these simulations, both ionic species were treated as Schottky defects, (see Section One of the **Extended Methods)**. Since our simulations assume that the mobile ionic species do not act as significant recombination centres, the only way in which the ionic and electronic charge are coupled is via Poisson's equation. This means that mobile ions only influence device performance by modulating the electrostatic potential and thus the spatial distribution of electronic carriers. Furthermore, since we consider the impact of ionic charge which is at quasi steady-state for the applied voltage, we can neglect any effects arising from a difference in the mobilities of the two species (although these effects would be significant if attempting to simulate e.g., V_{OC} transients). Consequently, the effects of adding a second ionic species are comparable to increasing the density of the pre-existing species by the same amount, though not identical due to the asymmetry between ionic accumulation and depletion regions.

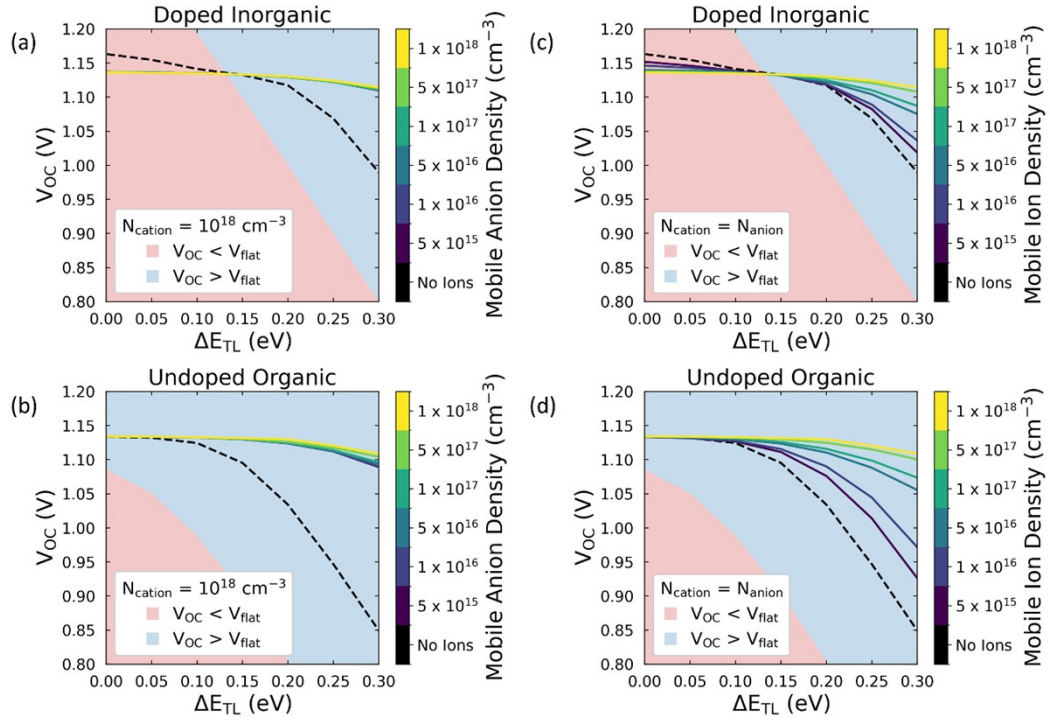

Figure S21: Figures (a-b) show the dependence of V_{OC} on ΔE_{TL} for doped inorganic (top) and undoped organic (bottom) parameter sets, assuming a constant cation density of 10^{18} cm^{-3} and a varying anion density. Figures (c-d) show the dependence of V_{OC} on ΔE_{TL} for doped inorganic (top) and undoped organic (bottom) parameter sets, assuming the cation and anion densities are equal. For all figures, the red and blue shaded regions indicate where V_{OC} is less than and greater than V_{flat}, respectively.

Supplementary Note Two

In this Supplementary Note, we consider the situation where the energetic offset to the transport layers, ΔE_{TL}, is not the same at the perovskite/HTL and perovskite/ETL interfaces. For concreteness, we will consider the case where the ETL has a fixed ΔE_{TL} of 0.15 eV and we vary ΔE_{TL} for the HTL as described in the main text. We chose this fixed value of ΔE_{TL} so that we could explore the cases where a given interface has both a larger and smaller energetic offset to the perovskite in a single parameter sweep. Additionally, we increased the surface recombination velocity to 100 cm s^{-1}, such that the recombination losses around V_{OC} are always dominated by surface recombination. We did this for two reasons: first, the case where bulk recombination dominates has already been discussed [29,30] and secondly, the model described in the main text is largely applicable to devices where surface recombination losses dominate. Furthermore, we use the doped inorganic parameter set to carry out these simulations to remove the additional complication of there being large voltage drops in the transport layers.

The results of our simulations for asymmetric ΔE_{TL} are shown in **Figure S22e**. First, we will discuss the novel phenomena which are observed under these conditions, and then we will consider how the model outlined in the main text must be adjusted to describe transport layer asymmetry and the validity of our experimental method under these conditions. The asymmetry of the transport layers' energetics results in an electronic carrier imbalance in the perovskite bulk where the nature of the carrier in excess (i.e., electron or hole) generally depends upon which transport layer has a smaller value of ΔE_{TL}. For example, in the case where the HTL is perfectly aligned with the perovskite valence band, there will be an excess of holes in the bulk of the perovskite, making it effectively p-type (see inset of **Figure S22a**). This behaviour occurs irrespective of the presence of a mobile ionic species, and generally results in worse overall device performance due to the reduced conductivity of the minority species, though an increase in V_{OC} can also be observed for devices limited by bulk recombination as the rate of this process is now determined by the minority carrier density.[29]

When mobile ions are present, the effective doping of the perovskite results in a non-zero excess ion density in the perovskite bulk (see **Figure S22a**). As our simulations assume that all the ionic charge is confined to the perovskite layer and that ionic charge is conserved, this results in the interfacial ionic accumulation and depletion regions containing unequal amounts of charge. Thus, the ionic accumulation/depletion regions on the two sides of the device no longer invert at the same applied bias (see Figures **S22c-d**). This means that there is no longer a single potential at which the ion distribution is uniform (i.e., V_{flat}), but instead two "inversion voltages". We have labelled these as V_{HTL} and V_{ETL}, respectively on **Figures S22c-e**. We note that these voltages were found to be almost independent of the mobile ion density (down to a mobile ion density of 10^{15} cm^{-3}). Additionally, in **Figure S22e**, we have drawn on the difference in the equilibrium values of the transport layers' Fermi energies, $\Delta E_{F,TLs}$ which is what determines the built-in potential for symmetric devices with highly doped transport layers (see main text). Interestingly, V_{ETL} and V_{HTL} are symmetrically distributed around $\Delta E_{F,TLs}$, with the offset decreasing as $\Delta E_{F,TLs}$ decreases. These facts will be of relevance when considering how asymmetry of the transport layers' energetics could affect the interpretation of our experimental data.

Considering these theoretical insights, we believe that the framework described in the main text is still applicable to a device with asymmetric contacts and where losses are dominated by surface recombination. However, in the asymmetric case, the effect of ions at each interface must be considered separately as the presence of ions will only reduce the minority carrier population at an interface compared to the case with no ions after the inversion voltage for that interface has been reached. Relative to a symmetric device with the same $\Delta E_{F,TLs}$, the inversion voltage will be below V_{flat} at the interface to the transport layer with the worse energetic alignment to the perovskite, and that at the opposite interface will be above V_{flat}. In the region between the two inversion voltages, surface recombination will only be supressed relative to the case with no mobile ions at one interface, namely

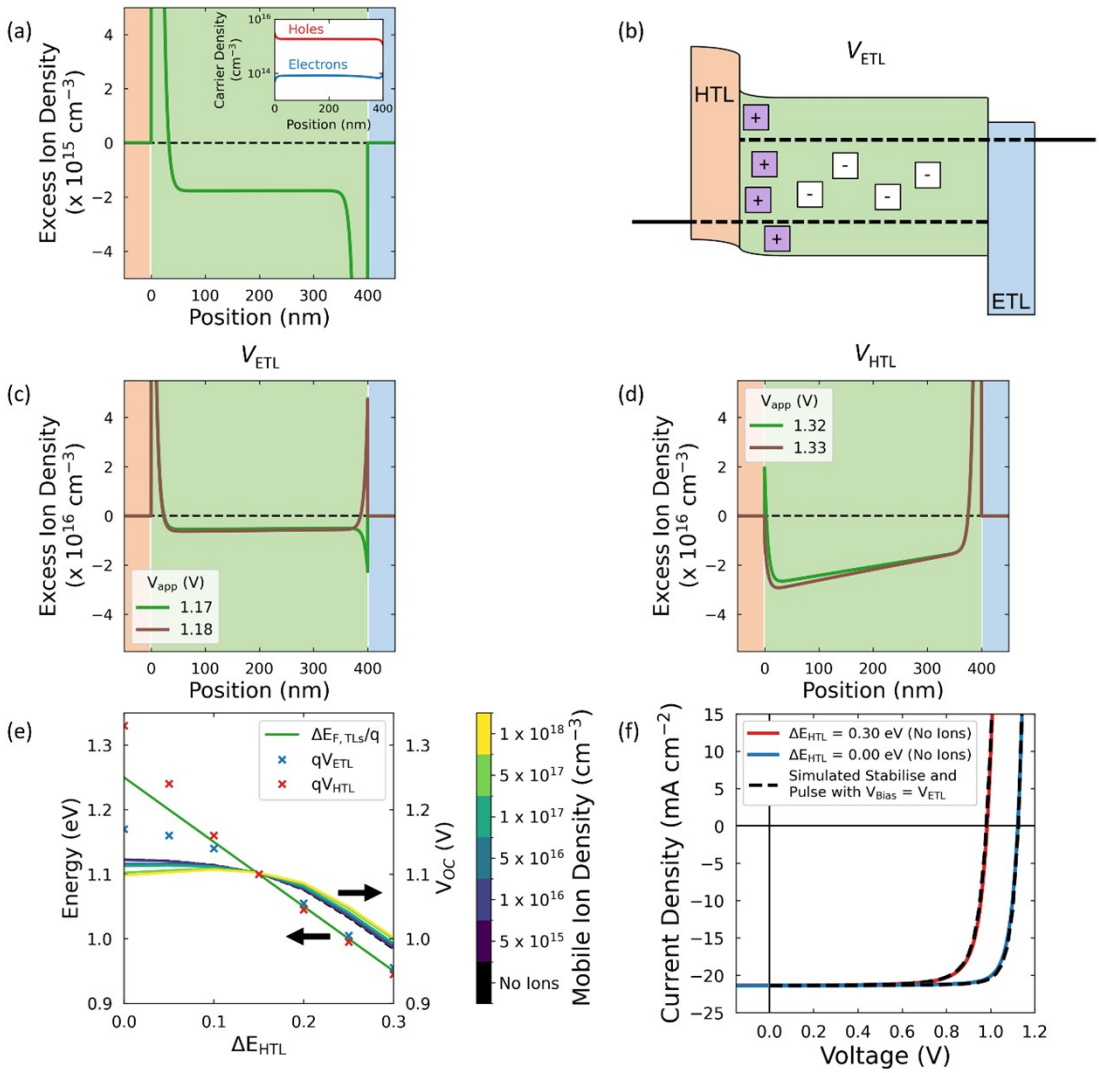

Figure S22: (a) Ionic and electronic carrier distributions at V_{OC} in the case where ΔE_{TL} is 0.15 eV at the perovskite/ETL interface and there is no offset at the perovskite/HTL interface. (b) Schematic band diagram at the voltage at which the ion population inverts at the perovskite/ETL interface (V_{ETL}) in the case where ΔE_{TL} is 0.15 eV at the perovskite/ETL interface and there is no offset at the perovskite/HTL interface. Inversion of the ionic population at (c) the perovskite/ETL interface and (d) the perovskite/HTL interface for the same device as shown in (a). Ionic inversion occurs at a lower applied voltage at the perovskite/ETL interface due to the excess hole density in the perovskite bulk. (e) V_{OC} as a function of ion density and energetic offset to the HTL (ΔE_{HTL}) for a fixed energetic offset to the ETL of 0.15 eV. We have also marked the difference in the equilibrium Fermi levels of the transport layers, ($\Delta E_{F,TLs}$) and the inversion voltages at the perovskite/ETL and perovskite/HTL interfaces (V_{ETL} and V_{HTL}, respectively). (f) Validation of the Stabilise and Pulse (SaP) measurement in the case of asymmetric energetic offsets to the transport layers. The parameters used are the same as those used to make figure (e) and, when ions have been included, we have used an ion density of 10^{18} cm^{-3}. The coloured lines show the JV curves obtained with the value of ΔE_{HTL} indicated in the legend and in the absence of mobile ions. The black dashed lines indicated the result of a simulated Stabilise and Pulse measurement performed at a prebias voltage equal to the inversion voltage at the interface with the worse energetic alignment (1.18 V for ΔE_{HTL} = 0.00eV and 0.94 V for ΔE_{HTL} = 0.30 eV). These agree well with the JVs obtained in the absence of mobile ions, showing that a Stabilise and Pulse measurement can still be used to probe the impact of ions on V_{OC} in the case of asymmetric transport layer energetics.

the one with worse energetic alignment to the perovskite. However, the voltage regimes above and below this intermediate region are analogous to the voltage being above and below V_{flat} in the symmetric case, respectively. This can be seen in our results as, for $\Delta E_{HTL} < 0.15$ eV, both V_{ETL} and V_{HTL} are above V_{OC}, meaning that the presence of mobile ions does not increase its value. Conversely, for $\Delta E_{HTL} > 0.15$ eV, both V_{ETL} and V_{HTL} are below V_{OC}, and thus V_{OC} increases in the presence of a mobile ionic species. The increase in V_{OC} due to mobile ions is not as large as is found in the symmetric case (see **Figure 1b**) as the effective doping of the perovskite layer due to the asymmetric contacts means that the distribution of the ionic charge no longer dominates the device's electrostatics. Thus, there is a smaller difference between the behaviour of the devices with and without ions.

Lastly, we consider the impact these findings have on our experimental data. If there is no single V_{flat} in the case where the transport layers have asymmetric energetic alignments, it is not obvious that *any* prebias potential will result in a pulsed JV which reproduces that of the ion-free device. Fortunately, our simulations suggest that the Stabilise and Pulse method is still viable as, in situations where there is an asymmetry in ΔE_{TL}, surface recombination is dominated by the interface with the worse energetic alignment (i.e., larger ΔE_{TL} value). Thus, in a device whose recombination current is largely limited by surface recombination, what matters in terms of the JV performance is the minority carrier density at the interface with the larger energetic offset between perovskite and the transport layer. This can be matched to the case with no mobile ions by applying a voltage prebias which corresponds to the flat ion potential on the side of the device with the larger ΔE_{TL}. In this case, our simulations suggest that the pulsed JV measurement will match the JV of an equivalent device with no mobile ions (see **Figure S22f**). As discussed above, the interface with the larger energetic offset will always have the lower inversion voltage and this will always be below $\Delta E_{F,TLs}$ meaning that it is highly likely this voltage will be included in the range of prebias values sampled in our measurements. Furthermore, in devices with larger energetic offsets to the transport layers (and hence lower values of $\Delta E_{F,TLs}$), our simulations suggest that there is not a large difference between V_{ETL} and V_{HTL}, implying that it may not be a bad approximation to assume a single V_{flat} in this situation.

Supplementary Note Three

In this Supplementary Note, we derive **Equation 1** in the main text, which gives an analytic expression for the change in electrostatic potential across the transport layers at the flat band condition in the perovskite, V_{flat}. In this derivation, the transport layers are treated as perfectly symmetric, undoped semiconductors, and we illustrate the geometry used in **Figure S23a**. In this figure, we have taken advantage of the fact that the electric field, E, at the perovskite/transport layer interfaces must be zero when we are at the flat band condition in the perovskite. This allows us to remove the perovskite layer from our consideration as its removal does not affect the boundary conditions for $V(x)$ at the newly formed ETL/HTL interface. By considering this diagram, we see that we can express the hole carrier density at position x in the hole transport layer (HTL) as

$$p(x) = N_V exp\left(\frac{E_V - \varphi - qV(x)}{k_B T}\right) \equiv n_0 exp\left(\frac{-eV(x)}{k_B T}\right) \tag{S1}$$

q is the electron charge, k_B is the Boltzmann constant, T is the temperature, N_V is the density of states at the valance band edge, E_V is the ionisation potential of the HTL, φ is the work function of the electrode and n_0 the carrier density in the transport layer at the interface with the electrode, which is as defined via $n_0 = N_V \exp\left[(E_V - \varphi)/k_B T\right]$. We can substitute this expression into Poisson's equation to yield

$$\frac{d^2V(x)}{dx^2} = -\frac{q}{\varepsilon\varepsilon_0} n_0 exp\left(\frac{-qV(x)}{k_B T}\right) \tag{S2}$$

ε is the permittivity of free space and ε_0 is the relative permittivity of the transport layers. By integrating this equation with respect to x, we can find the electric field, E, in the HTL

$$E(x) = -\frac{dV(x)}{dx} = \pm\sqrt{\frac{2n_0 q}{\varepsilon\varepsilon_0}\left(\frac{k_B T}{q} exp\left(\frac{-eV(x)}{k_B T}\right) - C\right)} \tag{S3}$$

C is a constant of integration, which can be found by using the following boundary conditions

$$E(x = w_{HTL}) = 0 \tag{S4}$$

$$V(x = w_{HTL}) = \frac{1}{2}(V_{BI} - V_{flat}) \equiv \frac{1}{2}\tilde{V} \tag{S5}$$

$$\Rightarrow C = \frac{k_B T}{q} exp\left(\frac{-q\tilde{V}}{2k_B T}\right) \tag{S6}$$

The first boundary condition follows from the fact we are trying to find an expression for the potential at which we reach the flat band condition in the perovskite and the second follows from the symmetry of the transport materials, which means that half of the total change in voltage occurs over the HTL. Additionally, from **Figure S23a**, we can see that the gradient of $V(x)$ is positive for all x, implying a negative electric field (i.e., holes move to the left). Thus, we can discard the positive root in **Equation S3**. We note that, due to the square root in **Equation S3**, this solution is only valid for $V < \tilde{V}$.

Following this, **Equation S3** can be integrated again to find that

$$D - x = \frac{k_B T}{q}\sqrt{\frac{2\varepsilon\varepsilon_0}{n_0 qC}} \arcsin\left(\sqrt{\frac{qC}{k_B T}} \exp\left(\frac{eV(x)}{2k_B T}\right)\right) \tag{S7}$$

D is a second constant of integration, which can be found by using the boundary condition

$$V(x = 0) = 0 \tag{S8}$$

$$\Rightarrow D = \frac{k_B T}{q}\sqrt{\frac{2\varepsilon\varepsilon_0}{n_0 qC}}arcsin\left(\sqrt{\frac{qC}{k_B T}}\right) \quad \text{(S9)}$$

By combining **Equations S3, S6 and S9**, we can write that

$$x = \sqrt{\frac{2\varepsilon\varepsilon_0 k_B T}{n_0 q^2}}exp\left(\frac{e\tilde{V}}{4k_B T}\right)\left[arcsin\left(exp\left(\frac{q(V(x)-\frac{1}{2}\tilde{V})}{2k_B T}\right)\right) - arcsin\left(exp\left(\frac{-q\tilde{V}}{4k_B T}\right)\right)\right] \quad \text{(S10)}$$

$$\Rightarrow w_{HTL} = \sqrt{\frac{2\varepsilon\varepsilon_0 k_B T}{n_0 q^2}}exp\left(\frac{e\tilde{V}}{4k_B T}\right)\left[\frac{\pi}{2} - arcsin\left(exp\left(\frac{-q\tilde{V}}{4k_B T}\right)\right)\right] \quad \text{(S11)}$$

as written in the main text. In **Figure S23b**, we plot the numerical solution for $\tilde{V}$ as a function of the energetic offset between the electrode work function and the HTL valance band using the transport layer parameters from the doped organic parameter set (see **Table S1**).

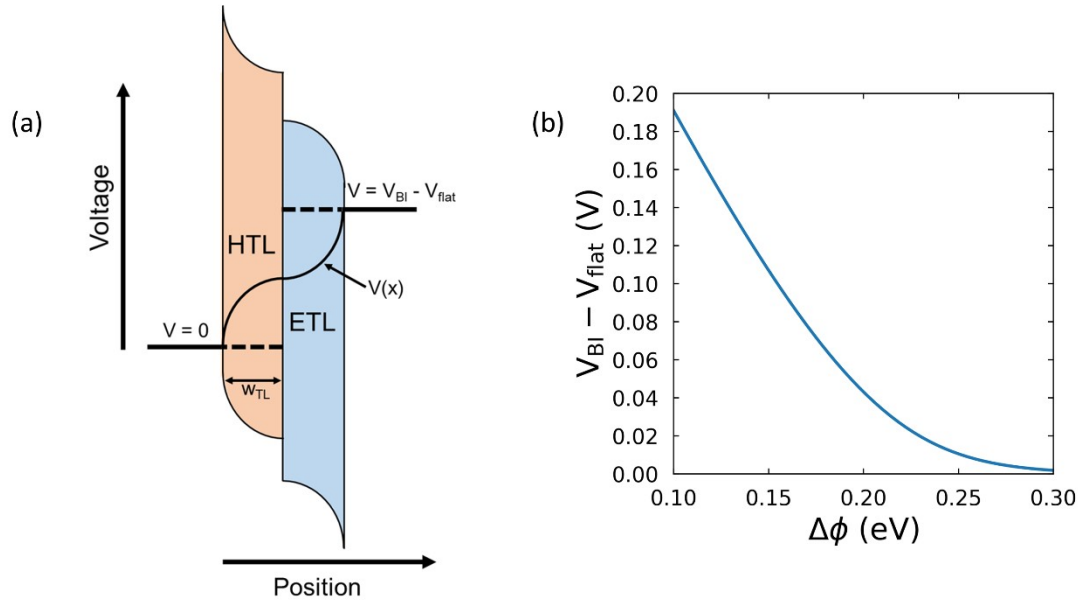

Figure S23: (a) Diagram of the geometry used to derive **Equation S10**. (b) Value of $\tilde{V} = V_{BI} - V_{flat}$ found using **Equation S11** as a function of the energetic offset between the work function of the electrode and the conduction (valance) band of the ETL (HTL), $\Delta\varphi$. This parameter controls the majority carrier density at the electrode/transport layer interfaces, N_0. The range of $\Delta\varphi$ shown here cover the range used in our simulation results, and the calculated offset between V_{BI} and V_{flat} agrees with that found using the full Driftfusion simulation (compare to **Figure S2**).

Supplementary Note Four

The simulations whose results are shown in **Figure 1** and **Figure 4** of the main text were performed on highly idealised perovskite devices. Thus, to verify that we would expect to see the same trends in real devices, we performed simulations using parameters representative of the Au/Spiro-OMeTAD/$MAPbI_3$/(C_{60}-BA)/TiO_2/FTO device stack (parameters given in **Table S6**). We modelled the effect of the C_{60}-BA by reducing the surface recombination velocity of holes at the perovskite/TiO_2 interface by a factor of one thousand. Although this may seem to be a simplistic treatment of the C_{60}-BA, we find that this change allowed us to recreate the observed trends in the Stabilise and Pulse measurements and the impact of mobile ions on V_{OC}, as is shown in **Figure S24**. JV parameters with and without mobile ions are given in **Table S7**, below.

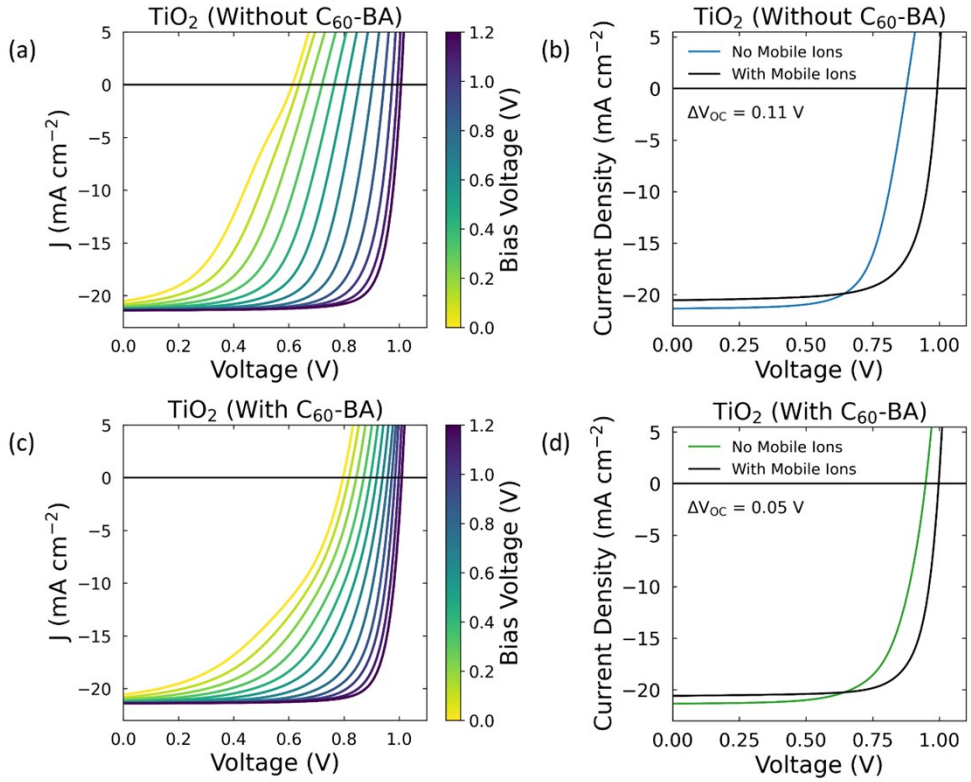

Figure S24: Simulated Stabilise and Pulse measurements (left-hand column) and JV curves with and without the inclusion of a mobile ionic species (right-hand column) for (a-b) devices without C_{60}-BA

and (c-d) devices with C_{60}-BA. Comparing this figure to **Figure 3** in the main text, we see that the simulations can accurately reproduce the experimental trends.

Device	With or Without Ions	J_{SC} (mA cm^{-2})	V_{OC} (V)	FF	PCE (%)
Without C_{60}-BA	With	20.50	0.99	0.73	14.9
	Without	21.30	0.88	0.70	13.0
With C_{60}-BA	With	20.60	1.00	0.76	15.7
	Without	21.20	0.95	0.69	13.9

Table S7: JV parameters from the JV curves shown in **Figure S23b** (without C_{60}-BA) and **Figure S23d** (with C_{60}-BA).

Supplementary Note Five

In this Supplementary Note, we summarise our Stabilise and Pulse measurements on Au/Spiro-OMeTAD/$MAPbI_3$/(C_{60}-BA)/SnO_2/FTO devices. As for the TiO_2 devices, we summarise the JV data in **Tables S8-9** and **Figure S25** (below). Additionally, on **pages 36-37**, we provide plots of the full Stabilise and Pulse measurements, $dJ/dV|_{V=Voc}$ versus V_{bias} and the quasi-steady state (QSS) and stabilise and pulse (SaP) JVs evaluated at V_{flat}. Plots of the full Stabilise and Pulse measurements include the polynomial fits used to evaluate $dJ/dV|_{V=Voc}$ (see **Methods**). Data is shown up to the highest V_{bias} necessary to determine the QSS V_{OC}.

Table S8: Summary of the JV parameters for the Au/Spiro-OMeTAD/$MAPbI_3$/SnO_2/FTO devices. JV parameters are given for three cases: as measured under the Solar Simulator using the protocol described in the **Methods** section (parameters taken from the reverse scan), as measured with the mobile ions at quasi-steady state (QSS JV) and as measured using Stabilise and Pulse measurements carried out at V_{bias} = V_{flat} (SaP JV). Additionally, we provide the value of V_{flat} extracted from our analysis of the Stabilise and Pulse data in column 2.

Device Number	V_{flat} (V)	Method	J_{SC} (mA cm^{-2})	V_{OC} (V)	FF	PCE (%)
1	0.68 ± 0.05	Solar Sim	21.30	1.053	0.75	16.82
		QSS JV	19.45	0.956	0.54	10.08
		SaP JV	21.77	0.826	0.64	11.47
2	0.68 ± 0.05	Solar Sim	21.50	1.054	0.71	16.11
		QSS JV	21.03	0.990	0.59	12.22
		SaP JV	21.45	0.848	0.66	12.03
3	0.67 ± 0.05	Solar Sim	21.49	1.031	0.73	16.09
		QSS JV	17.23	0.969	0.65	10.85
		SaP JV	21.38	0.789	0.62	10.46
4	0.65 ± 0.05	Solar Sim	20.51	1.033	0.73	15.51
		QSS JV	17.80	0.972	0.58	10.00
		SaP JV	20.20	0.771	0.62	9.59

Table S9: Summary of the JV parameters for the Au/Spiro-OMeTAD/$MAPbI_3$/C_{60}-BA/SnO_2/FTO devices. For further details, see the caption of **Table S8**.

Device Number	V_{flat} (V)	Method	J_{SC} (mA cm^{-2})	V_{OC} (V)	FF	PCE (%)

1	0.73 ± 0.05	Solar Sim	20.10	1.095	0.75	16.60
		QSS JV	19.24	1.042	0.75	14.96
		SaP JV	20.39	0.948	0.71	13.73
2	0.73 ± 0.05	Solar Sim	22.27	1.070	0.69	16.37
		QSS JV	20.61	0.977	0.72	14.42
		SaP JV	23.05	0.940	0.71	13.73
3	0.70 ± 0.05	Solar Sim	20.85	1.104	0.73	16.86
		QSS JV	20.75	1.012	0.74	15.57
		SaP JV	21.09	0.979	0.67	13.91
4	0.72 ± 0.05	Solar Sim	21.36	1.101	0.72	16.85
		QSS JV	21.08	1.029	0.77	16.70
		SaP JV	21.75	0.989	0.67	14.49

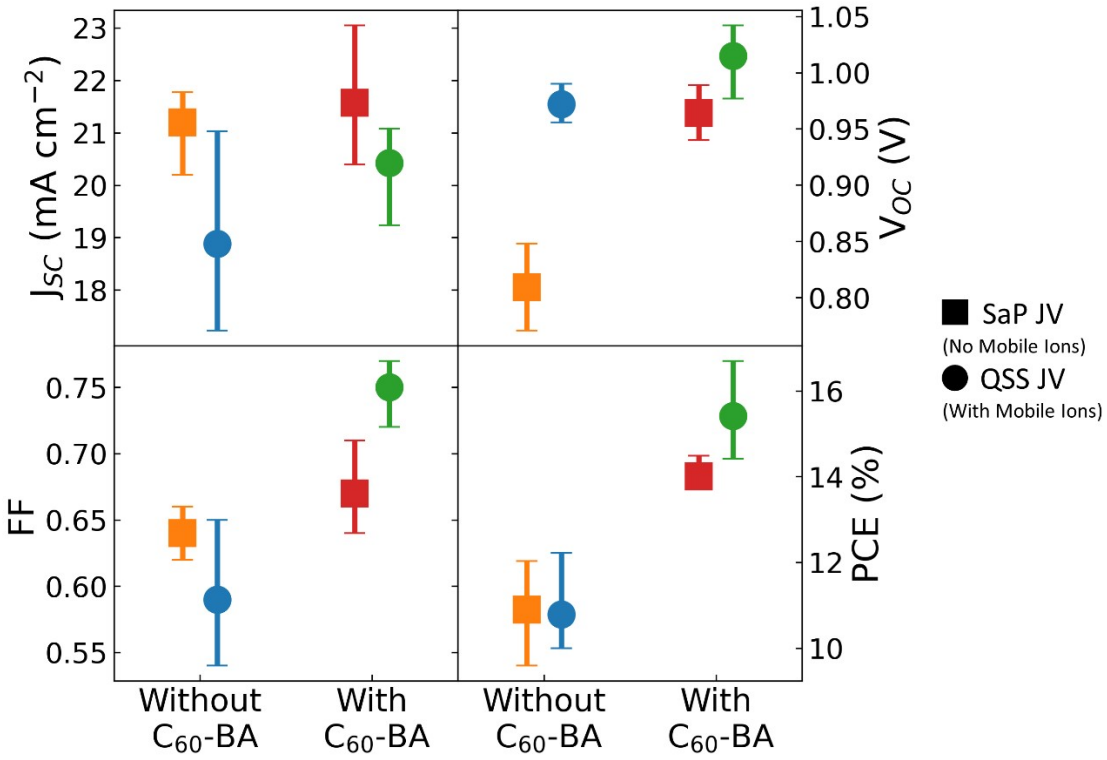

Figure S25: Summary of the JV parameters extracted from the Stabilise and Pulse (SaP) JVs and quasi-steady state (QSS) JVs for all measured SnO_2 devices. Error bars indicate the range of measured values. Considering the QSS JVs, we see that the inclusion of C_{60}-BA increases PCE and this is largely due to increases in J_{SC} and FF, as was observed in the TiO_2 devices (see **Figure 2e**). Furthermore, the devices using SnO_2 show the same trends in V_{OC} as the TiO_2 devices, namely that ions increase V_{OC} with and without the inclusion of C_{60}-BA, and the size of this improvement decreases when the C_{60}-BA is present. Additionally, in the devices with C_{60}-BA, we find that the presence of mobile ions increases PCE, as found in the TiO_2 devices. However, the devices without C_{60}-BA don't follow this trend, largely due to their low FF. This contrasts to what was observed in the TiO_2 devices, where the QSS JVs had higher FFs than the SaP JVs. By comparing the QSS JVs of the SnO_2 and TiO_2 devices without C_{60}-BA, we see that this difference originates from the rapid loss in photocurrent observed at low voltages in the SnO_2 devices. Since this behaviour is less pronounced in the devices with C_{60}-BA, we believe it is due to the interaction of the perovskite and SnO_2 layers. This highlights how well passivated interfaces are necessary for mobile ions to be beneficial to device performance.

SnO_2 (Without C_{60}-BA) – Device 1

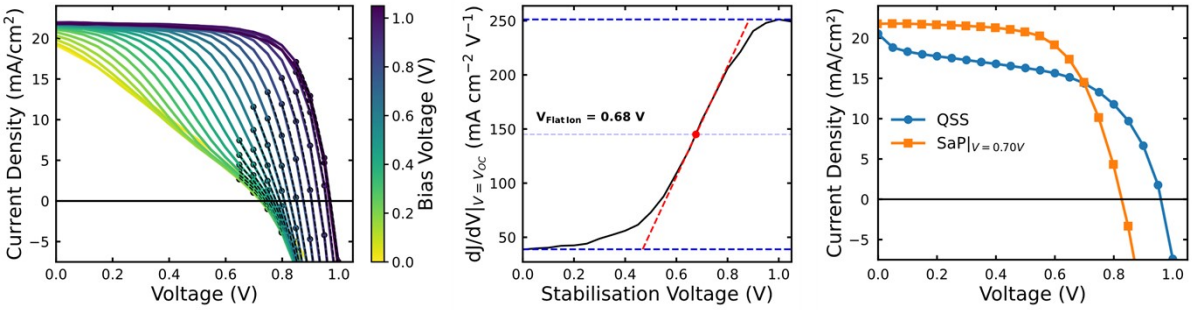

SnO_2 (Without C_{60}-BA) – Device 2

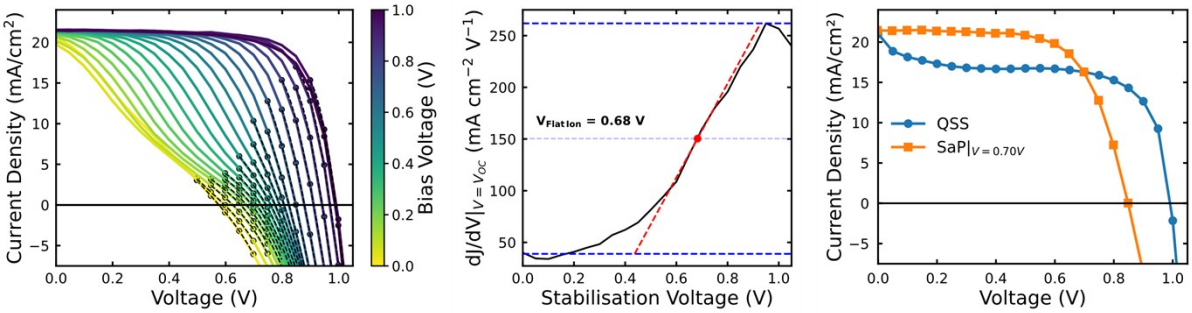

SnO_2 (Without C_{60}-BA) – Device 3

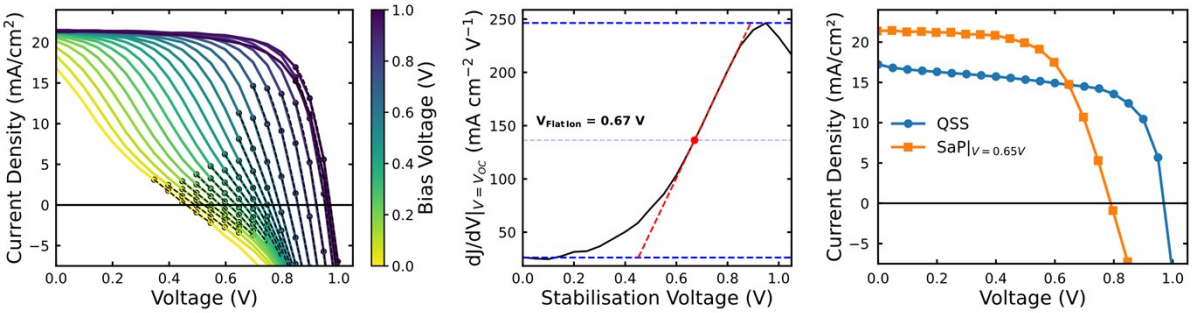

SnO_2 (Without C_{60}-BA) – Device 4

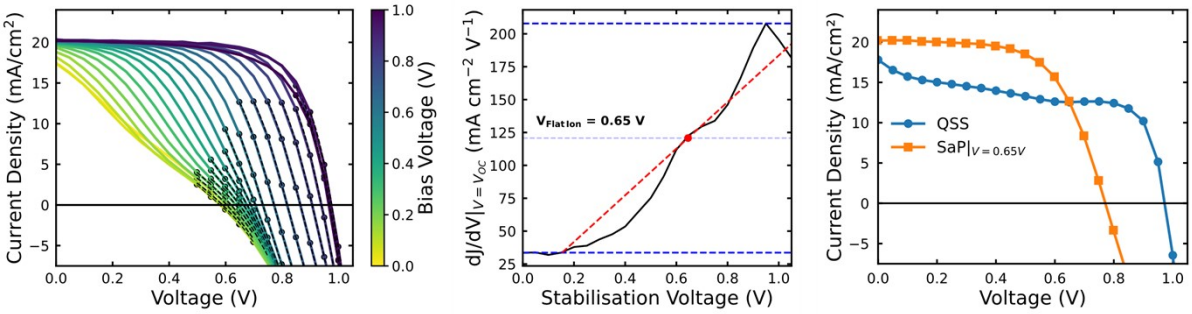

SnO_2 (With C_{60}-BA) – <u>Device 1</u>

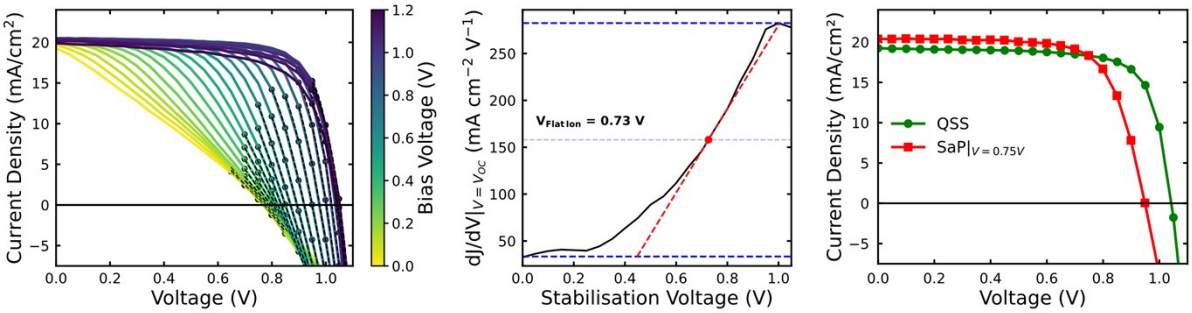

SnO_2 (With C_{60}-BA) – <u>Device 2</u>

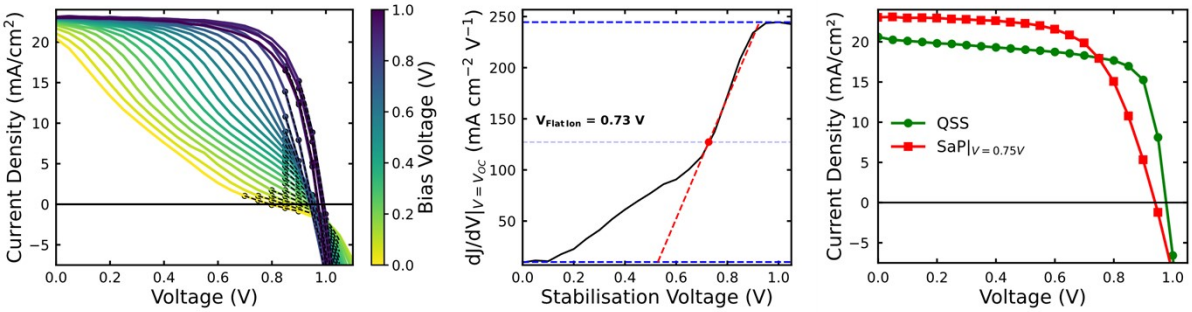

SnO_2 (With C_{60}-BA) – <u>Device 3</u>

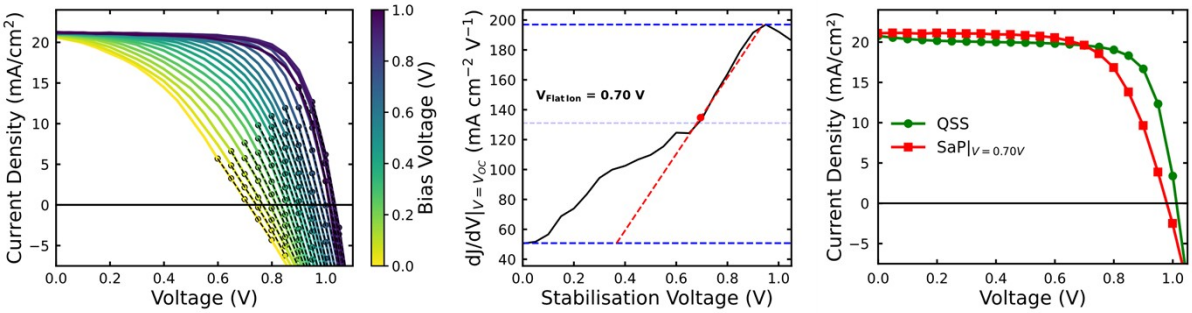

SnO_2 (With C_{60}-BA) – <u>Device 4</u>

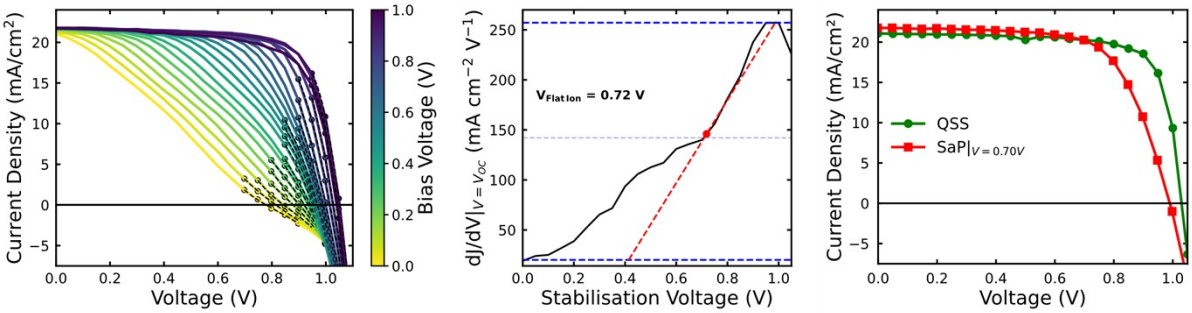

Supplementary Note Six

In this Supplementary Note, we provide additional data regarding the Stabilise and Pulse measurements carried out on the Au/Spiro-OMeTAD/$MAPbI_3$/(C_{60}-BA)/TiO_2/FTO devices which were not included in the main text. This data includes plots of the full Stabilise and Pulse measurements, $dJ/dV|_{V=Voc}$ versus V_{bias} and the quasi-steady state (QSS) and Stabilise and Pulse (SaP) JVs evaluated at V_{flat}. Plots of the full Stabilise and Pulse measurements include the polynomial fits used to evaluate $dJ/dV|_{V=Voc}$ (see **Methods**). Data is shown up to the highest V_{bias} necessary to determine the QSS V_{OC}.

TiO_2 (Without C_{60}-BA) – Device 2

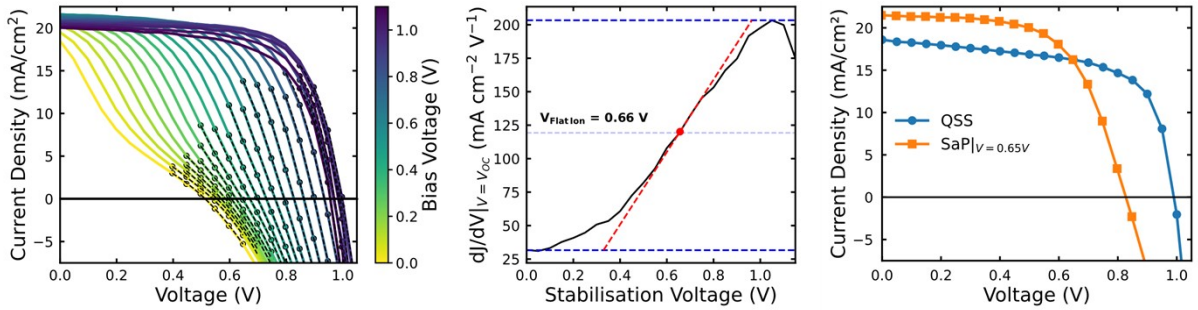

TiO_2 (Without C_{60}-BA) – Device 3

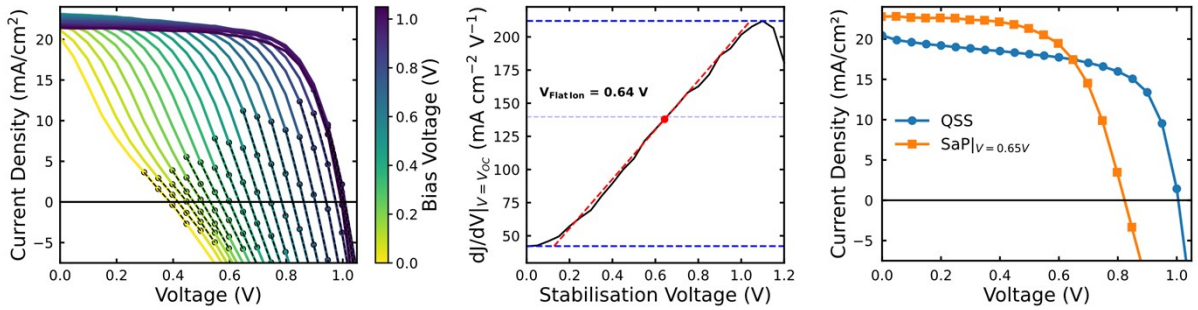

TiO_2 (Without C_{60}-BA) – Device 4

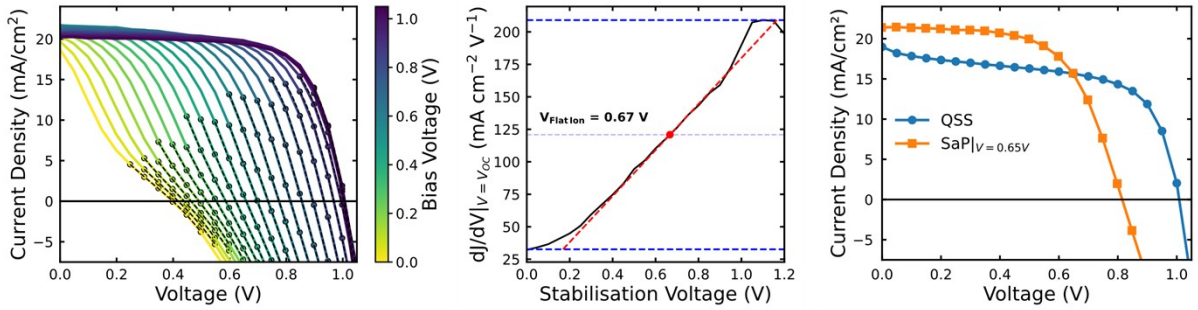

TiO_2 (Without C_{60}-BA) – Device 5

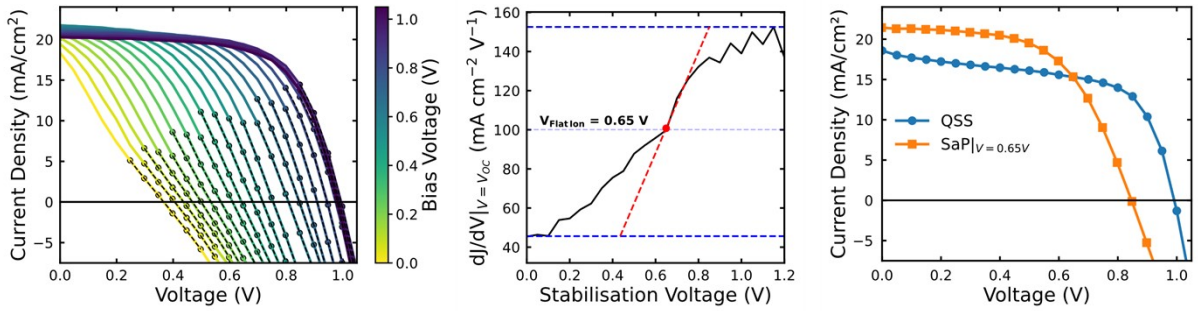

TiO_2 (With C_{60}-BA) – Device 1

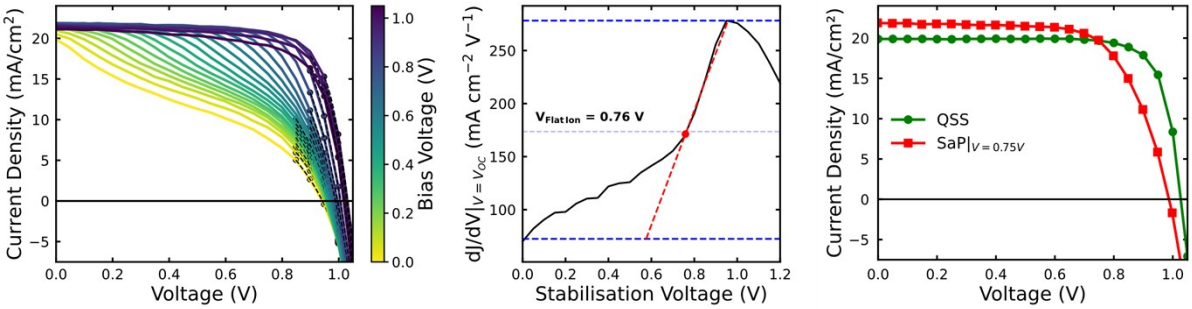

TiO_2 (With C_{60}-BA) – Device 2

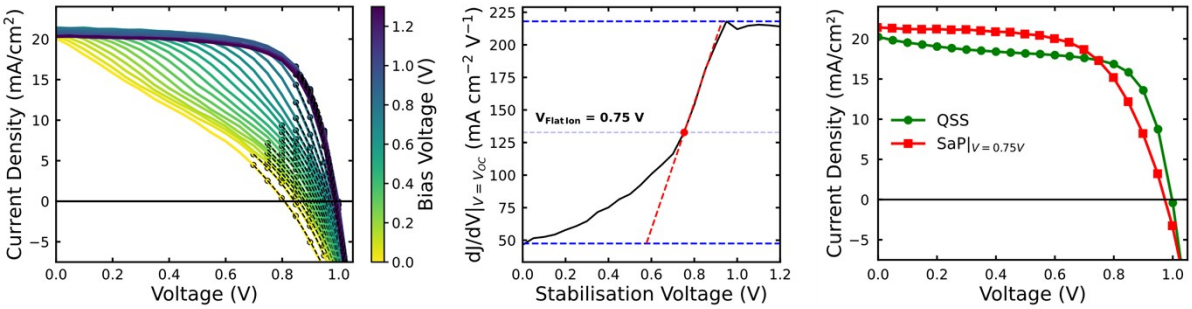

TiO_2 (With C_{60}-BA) – Device 3

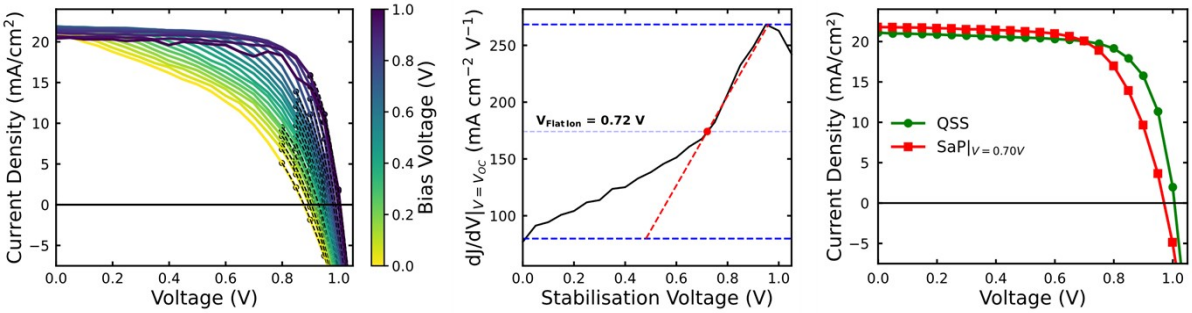

TiO_2 (With C_{60}-BA) – <u>Device 4</u>

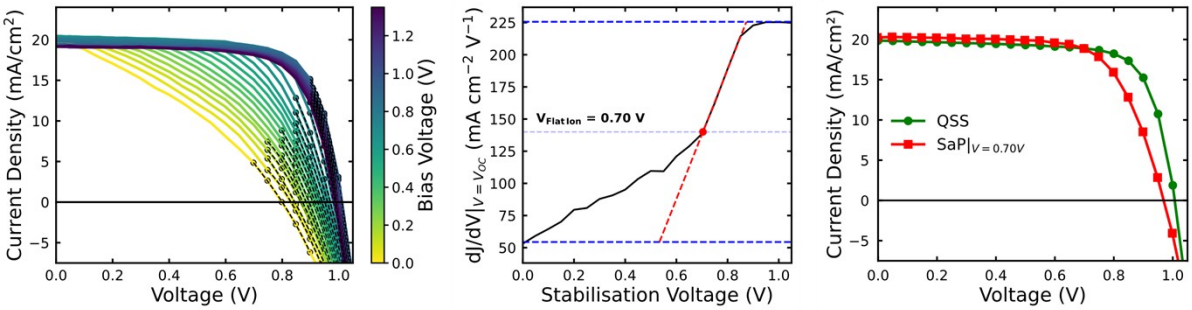

TiO_2 (With C_{60}-BA) – <u>Device 6</u>

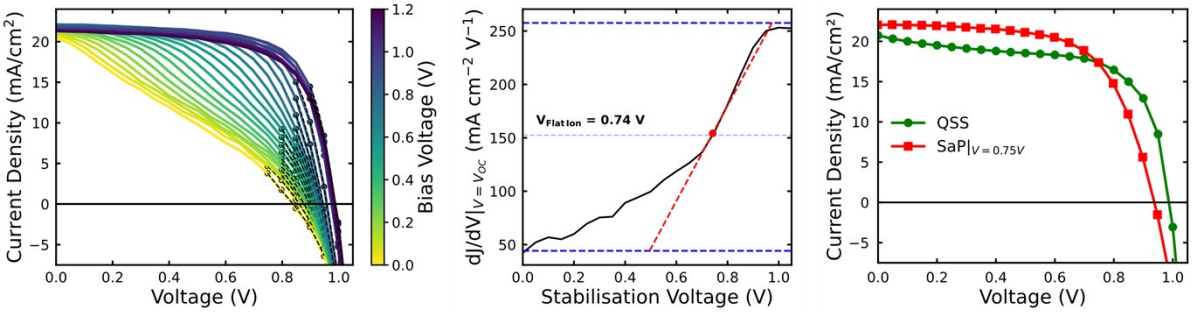

References

1. Yamada, Y., Nakamura, T., Endo, M., Wakamiya, A. & Kanemitsu, Y. Near-band-edge optical responses of solution-processed organic–inorganic hybrid perovskite $CH_3NH_3PbI_3$ on mesoporous TiO_2 electrodes. *Appl. Phys. Express* **7**, 032302 (2014).
2. Sharif, R. *et al.* A comprehensive review of the current progresses and material advances in perovskite solar cells. *Nanoscale Advances* **5**, 3803–3833 (2023).
3. Lim, J. *et al.* Long-range charge carrier mobility in metal halide perovskite thin-films and single crystals via transient photo-conductivity. *Nat Commun* **13**, 4201 (2022).
4. Stranks, S. D. *et al.* Electron-Hole Diffusion Lengths Exceeding 1 Micrometer in an Organometal Trihalide Perovskite Absorber. *Science* **342**, 341–344 (2013).
5. Kirchartz, T., Márquez, J. A., Stolterfoht, M. & Unold, T. Photoluminescence-Based Characterization of Halide Perovskites for Photovoltaics. *Advanced Energy Materials* **10**, 1904134 (2020).
6. Bertoluzzi, L. *et al.* Mobile Ion Concentration Measurement and Open-Access Band Diagram Simulation Platform for Halide Perovskite Solar Cells. *Joule* **4**, 109–127 (2020).
7. Leijtens, T. *et al.* Carrier trapping and recombination: the role of defect physics in enhancing the open circuit voltage of metal halide perovskite solar cells. *Energy Environ. Sci.* **9**, 3472–3481 (2016).
8. Wang, Y. *et al.* Improvement in the Performance of Inverted 3D/2D Perovskite Solar Cells by Ambient Exposure. *Solar RRL* **6**, 2200224 (2022).
9. Sánchez, J. G., Cabrera-Espinoza, A., Martínez-Ferrero, E., Delgado, J. L. & Palomares, E. Chalcogen-substituted PCBM derivatives as ternary components in PM6:Y6 solar cells. *Mater. Adv.* **3**, 1071–1078 (2022).
10. Mihailetchi, V. d. *et al.* Electron Transport in a Methanofullerene. *Advanced Functional Materials* **13**, 43–46 (2003).

11. Bässler, H., Kroh, D., Schauer, F., Nádaždy, V. & Köhler, A. Mapping the Density of States Distribution of Organic Semiconductors by Employing Energy Resolved–Electrochemical Impedance Spectroscopy. *Advanced Functional Materials* **31**, 2007738 (2021).
12. You, J. *et al.* Improved air stability of perovskite solar cells via solution-processed metal oxide transport layers. *Nature Nanotech* **11**, 75–81 (2016).
13. Zhang, B. *et al.* NiO/Perovskite Heterojunction Contact Engineering for Highly Efficient and Stable Perovskite Solar Cells. *Advanced Science* **7**, 1903044 (2020).
14. Rao, K. V. & Smakula, A. Dielectric Properties of Cobalt Oxide, Nickel Oxide, and Their Mixed Crystals. *Journal of Applied Physics* **36**, 2031–2038 (1965).
15. Xu, Y. *et al.* Ambient Processable and Stable All-Polymer Organic Solar Cells. *Advanced Functional Materials* **29**, 1806747 (2019).
16. Sun, J. *et al.* Inverted perovskite solar cells with high fill-factors featuring chemical bath deposited mesoporous NiO hole transporting layers. *Nano Energy* **49**, 163–171 (2018).
17. Rödl, C. & Schleife, A. Photoemission spectra and effective masses of n- and p-type oxide semiconductors from first principles: ZnO, CdO, SnO_2, MnO, and NiO. *physica status solidi (a)* **211**, 74–81 (2014).
18. Xu, W. *et al.* Asymmetric charge carrier transfer and transport in planar lead halide perovskite solar cells. *Cell Reports Physical Science* **3**, 100890 (2022).
19. Sławek, A., Starowicz, Z. & Lipiński, M. The Influence of the Thickness of Compact TiO_2 Electron Transport Layer on the Performance of Planar $CH_3NH_3PbI_3$ Perovskite Solar Cells. *Materials (Basel)* **14**, 3295 (2021).
20. Rombach, F. M., Haque, S. A. & Macdonald, T. J. Lessons learned from spiro-OMeTAD and PTAA in perovskite solar cells. *Energy Environ. Sci.* **14**, 5161–5190 (2021).
21. Scanlon, D. O. *et al.* Band alignment of rutile and anatase TiO_2. *Nature Mater* **12**, 798–801 (2013).
22. Safie, N. E., Azam, M. A., Aziz, M. F. A. & Ismail, M. Recent progress of graphene-based materials for efficient charge transfer and device performance stability in perovskite solar cells. *International Journal of Energy Research* **45**, 1347–1374 (2021).

23. Li, S., Cao, Y.-L., Li, W.-H. & Bo, Z.-S. A brief review of hole transporting materials commonly used in perovskite solar cells. *Rare Met.* **40**, 2712–2729 (2021).
24. Mi, Y. & Weng, Y. Band Alignment and Controllable Electron Migration between Rutile and Anatase TiO_2. *Sci Rep* **5**, 11482 (2015).
25. Wypych, A. *et al.* Dielectric Properties and Characterisation of Titanium Dioxide Obtained by Different Chemistry Methods. *Journal of Nanomaterials* **2014**, e124814 (2014).
26. Miao, F. *et al.* Force modulation of tunnel gaps in metal oxide memristive nanoswitches. *Applied Physics Letters* **95**, 113503 (2009).
27. Li, Z. *et al.* A facilely synthesized 'spiro' hole-transporting material based on spiro[3.3]heptane-2,6-dispirofluorene for efficient planar perovskite solar cells. *RSC Advances* **7**, 41903–41908 (2017).
28. Burschka, J. *et al.* Tris(2-(1H-pyrazol-1-yl)pyridine)cobalt(III) as p-Type Dopant for Organic Semiconductors and Its Application in Highly Efficient Solid-State Dye-Sensitized Solar Cells. *J. Am. Chem. Soc.* **133**, 18042–18045 (2011).
29. Wu, N., Walter, D., Fell, A., Wu, Y. & Weber, K. The Impact of Mobile Ions on the Steady-State Performance of Perovskite Solar Cells. *J. Phys. Chem. C* **124**, 219–229 (2020).
30. Córdoba, M. & Taretto, K. Insight into the Dependence of Photovoltaic Performance on Interfacial Energy Alignment in Solar Cells with Mobile Ions. *Solar RRL* **8**, 2300742.